J. Fluid Mech. (2003), *vol.* 482, *pp.* 17–50. © 2003 Cambridge University Press
DOI: 10.1017/S0022112003003987 Printed in the United Kingdom

Vortex instability in a diverging–converging channel

By J. M. FLORYAN

Department of Mechanical and Materials Engineering, The University of Western Ontario, London, Ontario, N6A 5B9, Canada

(Received 15 November 2001 and in revised form 20 November 2002)

Linear stability of flow in a diverging–converging channel is considered. The flow may develop under either the fixed mass or the fixed pressure gradient constraint. Both cases are considered. It is shown that under certain conditions the divergence–convergence of the channel leads to the formation of a secondary flow in the form of streamwise vortices. It is argued that the instability is driven by centrifugal effect. The instability has two modes and conditions leading to their onset have been identified. These conditions depend on the amplitude and the length of the channel diverging–converging section and can be expressed in terms of a critical Reynolds number. The global critical conditions describing the minimum critical Reynolds number required to create the instability for the specified amplitude of the variations of the channel opening are also given. It is shown that the flow developed under the fixed mass constraint is slightly more unstable than the flow developed under the fixed pressure constraint. This difference increases with an increase of the amplitude of the channel divergence–convergence.

1. Introduction

It is well known that turning shear layers are subject to an instability that, under certain conditions, gives rise to a secondary flow in the form of streamwise vortices. It is also known that the centrifugal force field drives this instability. This instability has been studied in the case of simple geometries and reference canonical flows where the curvature of streamlines can be predicted and/or approximated easily. Rayleigh (1920) studied the inviscid mechanism in the case of flow between rotating cylinders and was able to determine the necessary stability condition; this condition is expressed in terms of distribution of circulation. Taylor (1923) considered the full viscous problem and determined the critical conditions for the onset of the secondary flow. Dean (1928) analysed similar instability in a curved channel. Görtler (1941) demonstrated the existence of centrifugal instability in the case of boundary layers over concave surfaces. Floryan (1986) showed that the instability is active in flows over concave as well as convex surfaces if the streamwise velocity distribution is non-monotonic. All of these studies are similar in the sense that wall curvature is (or can be considered as) constant, permitting description of the critical stability conditions in terms of a single parameter.

The present work is focused on flows in diverging–converging channels. Variations of channel geometry force the flow to change direction, i.e. to expand and to contract, resulting in the creation of a centrifugal force field that may potentially drive the instability.

The diverging–converging channels have been studied in the context of search for better heat transfer augmentation schemes. Such schemes can be divided broadly into two categories, i.e. methods involving changes in effective thermophysical properties and methods involving improved mixing (Bergless & Webb 1985). Mixing is defined here as exchange of mass in the direction normal to the channel wall. Improved mixing is of special interest in compact heat exchangers operating at low Reynolds numbers where the flow is laminar and difficult to mix. Improved mixing can be obtained by forcing laminar–turbulent transition under subcritical conditions or by using various forms of vortex generators (Fiebig & Chen 1999) (but with a rather large pressure drag penalty). One class of mixing augmentation methods relies on hydrodynamic instabilities of separated shear layers (Patera & Mikic 1986). A set of transverse grooves is created on the channel wall in such a way that flow separates between the grooves. The flow is then driven with a small oscillatory component that enters into resonance with separated shear layers.

Centrifugal instability represents an alternative hydrodynamic instability augmentation method. It creates streamwise vortices without the large drag penalty associated with the standard vortex generators. Its effective use depends on the complete understanding of the conditions under which it is strongest. Even when the flow is marginally stable, the instability may assist the standard vortex generators in reducing the decay rate of the vortices and thus reducing the required number of such generators. The instability may occur only if the walls are properly shaped. Flow separation between channel contractions is undesired as it changes the effective centrifugal force field.

The existence of streamwise vortices attributed to centrifugal instability in channels with variable geometry has been confirmed experimentally by Gschwind, Regele & Kottke (1995) and Nishimura *et al.* (1990*a*). This confirmation is only qualitative as these authors studied channels of geometry different from the one being of interest here.

Characteristics of two-dimensional flows in diverging–converging channels have been studied by Nishimura *et al.* (1984, 1985, 1986, 1990*b*) and Wang & Vanka (1995) under flow and geometric conditions, leading to a very large flow separation in the expanded section of the channel. These authors, as well as Mendes & Sparrow (1984) in the case of tubes, observed improvement in flow mixing, although it was not attributed to any well-defined flow phenomenon.

The existing theoretical analyses have been focused on flows over wavy surfaces. Craik (1982) and Leibovich (1977) considered three-dimensional instability of shear layers over wavy interfaces giving rise to streamwise vortices in the context of Langmuir circulation. The analysis was simplified by taking advantage of the small amplitude of the waves and relied on averaging techniques. The resulting vortices were attributed to the action of centrifugal effect and the corresponding mechanism is referred to as the CL2 mechanism (Leibovich 1983). The CL2 mechanism can also operate in a non-centrifugal regime as shown by Phillips & Wu (1994) in the case of uniform shear between two wavy walls and by Phillips, Wu & Lumley (1996) in the case of turbulent boundary layers over a wavy terrain. The necessary conditions for such instability are expressed in terms of the Craik–Phillips–Shen criterion (see review by Phillips 1998). Experiments of Gong, Taylor & Dörnbrack (1996) confirmed the existence of this instability in the case of turbulent boundary layers. Saric & Benmalik (1991) analysed the boundary layer over a wavy surface and concluded that the centrifugal mechanism was not important for their flow conditions. Floryan (2002) considered Couette flow in the same geometry and identified the conditions necessary for the generation of the vortices.

The properties of flows in diverging–converging channels are also of interest from a fundamental point of view, i.e. how the variations in channel geometry affect the laminar–turbulent transition process. Guzman & Amon (1994, 1996) and Amon, Guzman & Morel (1996) considered channels with very large expansions and identified numerous possible responses of the resulting dynamical system. Their analysis was limited to two dimensions and thus was unable to capture possible formation of streamwise vortices.

Centrifugal instability is of interest as it may give rise to a bypass transition. This process involves rapid three-dimensionalization of the flow field, formation of transverse shear layers with inflection points and rapid growth of secondary instabilities (Floryan 1991). As a result, centrifugal instability may be used as a method for improvement of mixing through initiation of subcritical transition.

Presence of channel divergence–convergence may lead to interesting modifications of properties of turbulent flow. Hudson, Dykhno & Hanratty (1996) carried out extensive experimental measurements in a flow over a wavy wall and concluded that the structure of turbulence was fundamentally different in the wall layer and was related to the properties of separating shear layers. Direct numerical simulations of Cherukat *et al.* (1998) confirmed most of these observations. Simulations of De Angelis, Lombardi & Banerjee (1997) identified turbulent structures that resembled streamwise vortices. Nakagawa & Hanratty (2001) observed some structures in their experiments, but have not identified their properties.

The magnitude and distribution of the centrifugal force field in the channel depends on the shape of the converging and diverging sections. Because of variations of channel geometry in the axial direction, this field requires a minimum of two parameters for its characterization. The first parameter is the difference between the widest and the narrowest channel openings and the second is the distance between the corresponding points on the channel axis. It is convenient for the purposes of this analysis to define a reference diverging–converging channel where the shape of the walls is described by simple sine functions. The change in the channel opening is then expressed in terms of the amplitude of these functions, and the distance between the narrowest and the widest sections is expressed in terms of the wavelength. As the centrifugal force field changes from stabilizing to destabilizing along the channel axis, the critical instability conditions depend on whether the driving mechanism in the area where the force field is destabilizing (converging section) is strong enough to drive the secondary motion in the area where this field is stabilizing (diverging section).

It is expected that the flow may become unstable for various combinations of the two parameters discussed above, with the value of the critical Reynolds number being different in each case. This critical value will be determined using linear stability theory, and its variations as a function of the channel geometry will be sought. Since the onset of the instability is of interest, the analysis will focus on the amplitudes of channel divergence–convergence that are just large enough to induce instability. The global critical Reynolds number, where the flow does not become unstable for the specified contraction of the channel regardless of its wavelength, is also sought. The analysis is focused primarily of the low Reynolds numbers where the flow is expected to be stable with respect to travelling waves and the centrifugal effect offers the most plausible mechanism for flow modification. Such conditions are of primary interest in the design of heat exchangers.

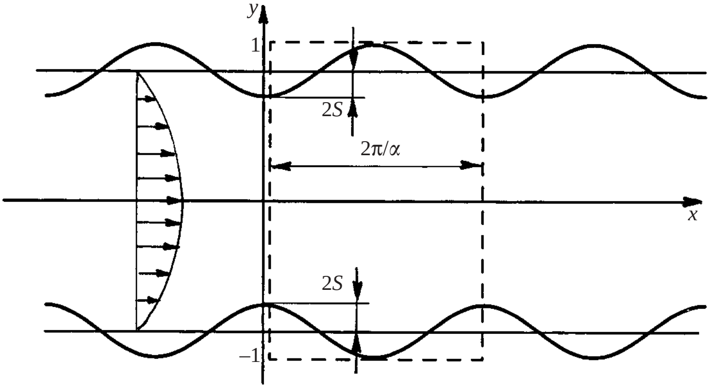

FIGURE 1. Sketch of the flow domain. The computational domain is contained between $y=-1-2S$ and $y=1+2S$.

The paper is organized as follows. Section 2 describes the form of the flow in a diverging–converging channel. Section 3 describes the linear stability analysis of this flow. Results of the analysis are discussed in §4. Section 5 provides a short summary of the main conclusions.

2. Flow in a diverging–converging channel

The section is devoted to the determination of the form of the basic state, i.e. the form of a two-dimensional, steady flow in a diverging–converging channel. There are infinitely many possible variations of geometry of a diverging–converging channel. In order to focus our analysis, we shall consider the simplest reference case, i.e. a channel whose walls are described by simple sine functions, as shown in figure 1. More complex channels can be described by a superposition of such functions, resulting in a geometry described by a Fourier expansion. The present channel can be viewed as representing the first term of such an expansion. Accordingly, the shapes of the upper and lower walls, $y_U(x)$ and $y_L(x)$, are given as (see figure 1)

$$\left.\begin{aligned} y_U(x) &= 1+(-S\mathrm{e}^{\mathrm{i}\alpha x}+\text{c.c.}), \\ y_L(x) &= -1+(S\mathrm{e}^{\mathrm{i}\alpha x}+\text{c.c.}), \end{aligned}\right\} \tag{2.1}$$

where S is real and denotes the amplitude of the wall corrugation, α is real and stands for the wavenumber of the corrugation and c.c. stands for the complex conjugate. The flow domain is bounded by $-\infty < x < \infty$, $(-1-2S) \leqslant y \leqslant (1+2S)$. The change in the channel opening owing to its divergence–convergence, from the largest opening to the smallest, is $8S$.

The goal of this analysis is the establishment of the critical conditions leading to the onset of the instability. Our interest is therefore in the determination of the smallest change in the channel opening that results in the generation of a secondary motion. The problem of description of the basic state, i.e. flow in a channel shown in figure 1, can thus be posed as a problem of determination of the modifications to the flow in a straight channel occurring due to the addition of the channel divergence–convergence.

Consider plane Poiseuille flow confined between flat rigid walls at $y=\pm 1$ and extending to $\pm\infty$ in the x-direction (figure 1). The fluid motion is described by the velocity and pressure fields in the form

$$\boldsymbol{V}_0(\boldsymbol{x}) = [u_0(x, y), v_0(x, y)] = [u_0(y), 0] = [1 - y^2, 0], \quad p_0(\boldsymbol{x}) = -2x/Re, \tag{2.2}$$

where the fluid is directed towards the positive x-axis and the Reynolds number Re is defined on the basis of the maximum x-velocity and the half-channel height.

Flow in the diverging–converging channel can be represented as

$$\begin{gathered} \boldsymbol{V}(\boldsymbol{x}) = [u(x, y), v(x, y)] = \boldsymbol{V}_0(\boldsymbol{x}) + \boldsymbol{V}_1(\boldsymbol{x}) = [u_0(y), 0] + [u_1(x, y), v_1(x, y)], \\ p(\boldsymbol{x}) = p_0(\boldsymbol{x}) + p_1(\boldsymbol{x}), \end{gathered} \tag{2.3}$$

where $\boldsymbol{V}_1$ and p_1 are the velocity and pressure modifications due to the channel divergence–convergence. Substitution of the above representation of the flow quantities into the Navier–Stokes and continuity equations, introduction of stream function defined as $u_1 = \partial_y \Psi$, $v_1 = -\partial_x \Psi$, and elimination of pressure permit expression of the field equations in the form

$$(u_0 \partial_x + \partial_y \Psi \, \partial_x - \partial_x \Psi \, \partial_y) \nabla^2 \Psi - \mathrm{D}^2 u_0 \partial_x \Psi = \frac{1}{Re} \nabla^4 \Psi, \tag{2.4}$$

where $\mathrm{D} = \mathrm{d}/\mathrm{d}y$. Since u_1 and v_1 are periodic in x with the period $\lambda = 2\pi/\alpha$, the stream function can be represented as

$$\Psi(x, y) = \sum_{n=-\infty}^{n=+\infty} \Phi_n(y) \, \mathrm{e}^{\mathrm{i}n\alpha x} \tag{2.5}$$

where $\Phi_n = \Phi_{-n}^*$ and asterisk denotes complex conjugate. In general, we cannot exclude the possibility of the existence of subharmonics in the velocity field. Their presence, however, can be accounted for by a simple change of indices in (2.5). No subharmonics were found in the parameter range subject to this investigation.

The functions Φ_n, $n \geqslant 0$, in (2.5) are governed by a nonlinear system of ordinary differential equations in the form

$$\left[\mathrm{D}_n^2 - \mathrm{i}n\alpha Re(u_0 \mathrm{D}_n - \mathrm{D}^2 u_0)\right] \Phi_n - \mathrm{i}\alpha Re \sum_{k=-\infty}^{k=+\infty} [k \, \mathrm{D}\Phi_{n-k} \mathrm{D}_k \Phi_k - (n-k) \Phi_{n-k} \mathrm{D}_k \mathrm{D}\Phi_k] = 0, \tag{2.6}$$

where $\mathrm{D}_n = \mathrm{D}^2 - n^2\alpha^2$. Equation (2.6) was obtained through substitution of (2.5) into (2.4) and separation Fourier components.

The boundary conditions at the channel walls are expressed in the following form

$$u_0(y_U(x)) + u_1(x, y_U(x)) = 0, \quad v_1(x, y_U(x)) = 0, \tag{2.7a}$$

$$u_0(y_L(x)) + u_1(x, y_L(x)) = 0, \quad v_1(x, y_L(x)) = 0. \tag{2.7b}$$

Specifying one additional condition closes the problem formulation. This condition arises because an x-periodic velocity field may be associated with a pressure field that has a component linear in x. Note that introduction of the channel divergence–convergence increases resistance to the flow as compared to a straight channel. Thus, if the flow is driven by the same mean pressure gradient, the volume flux has to decrease. Alternatively, if we want to maintain the same volume flux, the mean pressure gradient must increase. The additional condition can be cast either in terms of the volume flux or in terms of the pressure gradient. Both types of constraint have been investigated in this analysis.

The fixed mass condition involves only kinematic characteristics of the flow and can be conveniently cast in terms of streamfunction in the form

$$\Psi_0(y_L(x)) + \Psi(x, y_L(x)) = 0, \tag{2.8}$$

$$\Psi_0(y_U(x)) + \Psi(x, y_U(x)) = \tfrac{4}{3}, \tag{2.9}$$

where $\Psi_0 = -\frac{1}{3}y^3 + y + \frac{2}{3}$ denotes the streamfunction of the Poiseuille flow (continued analytically in $-1 - 2S < y < 1 + 2S$). Condition (2.8) is associated with the use of the streamfunction and has been selected arbitrarily.

The determination of the fixed pressure condition requires explicit writing of an equation for Φ_0. This equation is obtained from (2.6) with $n = 0$ and, after some rearrangements, it takes the form

$$\mathrm{D}^4\Phi_0 + 2\alpha Re\,\mathrm{Im}\left[\sum_{k=1}^{k=+\infty} k\mathrm{D}^2(\Phi_k^*\mathrm{D}\Phi_k)\right] = 0, \tag{2.10}$$

where Im denotes the imaginary part. Single integration of (2.10) gives

$$\mathrm{D}^3\Phi_0 + 2\alpha Re\,\mathrm{Im}\left[\sum_{k=1}^{k=+\infty} k\mathrm{D}(\Phi_0^*\mathrm{d}\Phi_k)\right] = \mathrm{A}\,Re. \tag{2.11}$$

It can be shown that the constant of integration A describes the mean pressure gradient induced by the channel divergence–convergence, i.e.

$$\partial p_1/\partial x|_{n=0} = \mathrm{A}. \tag{2.12}$$

This is done by taking the x-momentum equation, substituting (2.3) and (2.5), extracting from the pressure field mode corresponding to $n = 0$ and rearranging the resulting expression.

The condition expressing the fixed pressure gradient constraint is expressed by (2.11) with $\mathrm{A} = 0$. This condition can be enforced at any value of y inside the flow domain. Equation (2.8) remains as an arbitrary condition associated with the introduction of the streamfunction.

2.1. *Numerical solution*

The problem to be solved numerically consists of an infinite system of nonlinear ordinary differential equations, (2.6), subject to boundary conditions (2.7)–(2.8) and either constraint (2.9) or (2.11). Since the flow domain is limited in the y-direction by two lines that are functions of x, the computational domain is regularized by extending it to $y \in \langle -1 - 2S, 1 + 2S\rangle$.

The representation of the streamfunction of the flow modifications Ψ is truncated to M leading Fourier modes, i.e.

$$\Psi\,(x, y) \approx \sum_{n=-M}^{n=M} \Phi_n(y)\mathrm{e}^{\mathrm{i}n\alpha x}. \tag{2.13}$$

The corresponding, finite dimensional system of the ordinary differential equations for the functions Φ_n, $n = 0, 1, \ldots, M$ can be written easily on the basis of (2.6). This system can be discretized with spectral accuracy by introducing Chebyshev representations of the unknown function Φ_n as follows

$$\Phi_n(y) = \sum_{j=0}^{j=\infty} G_j^n T_j(y) \approx \sum_{j=0}^{j=K} G_j^n T_j(y), \tag{2.14}$$

where T_j denotes the Chebyshev polynomial of the jth order defined in $y \in (-1-2S, 1+2S)$ and G_j^n stands for the unknown expansion coefficient. The $M^*(K-4)$ algebraic equations for G_j^n are obtained through application of the tau technique. The remaining $4M$ equations are to be obtained from the flow boundary conditions.

Implementation of boundary conditions relies on the concept of immersed boundary conditions developed by Szumbarski & Floryan (1999) and will be discussed in the context of the lower wall. The following presentation is limited to a short outline. We begin by evaluating velocity components $u_L(x) = u(x, y_L(x))$ and $v_L(x) = v(x, y_L(x))$ along the lower wall represented by (2.1). Both velocity components u_L and v_L are x-periodic and thus can be expressed in terms of Fourier series as

$$u_L(x) \equiv u(x, y_L(x)) = \sum_{n=-M}^{n=M} (U_n)_L \, \mathrm{e}^{\mathrm{i}n\alpha x}, \quad v_L(x) \equiv v(x, y_L(x)) = \sum_{n=-M}^{n=M} (V_n)_L \, \mathrm{e}^{\mathrm{i}n\alpha x}. \tag{2.15}$$

The same velocity components can also be expressed using the assumed form of the solution, i.e.

$$u_L(x) \cong u_0(y_L(x)) + \sum_{n=-M}^{n=M} \mathrm{D}\Phi_n(y_L(x))\mathrm{e}^{\mathrm{i}n\alpha x} = u_0(y_L(x)) + \sum_{n=-M}^{n=M} \sum_{j=0}^{j=K} G_j^n \, \mathrm{D}T_j(y_L(x))\mathrm{e}^{\mathrm{i}n\alpha x}$$

$$v_L(x) \cong -\mathrm{i}\alpha \sum_{n=-M}^{n=M} n\Phi_n(y_L(x))\mathrm{e}^{\mathrm{i}n\alpha x} = -\mathrm{i}\alpha \sum_{n=-M}^{n=M} \sum_{j=0}^{j=K} nG_j^n \, T_j(y_L(x))\mathrm{e}^{\mathrm{i}n\alpha x}. \tag{2.16}$$

Since values of Chebyshev polynomials evaluated at $y = y_L(x)$ are periodic functions of x, they can be represented as

$$T_j(y_L(x)) = \sum_{k=-\infty}^{k=\infty} \left(w_k^j\right)_L \mathrm{e}^{\mathrm{i}k\alpha x}, \quad \mathrm{D}T_j(y_L(x)) = \sum_{k=-\infty}^{k=\infty} \left(d_k^j\right)_L \mathrm{e}^{\mathrm{i}k\alpha x}. \tag{2.17}$$

Insertion of (2.17) into (2.16) and separation of Fourier modes results in the explicit expressions for coefficients of Fourier expansions (2.15), leading to boundary conditions (2.7*b*) in the form

$$U_n = (F_n)_L + \sum_{m=-M}^{m=M} \sum_{j=0}^{j=K} \left(d_{n-m}^j\right)_L G_j^m = 0, \quad M \geqslant n \geqslant 0, \tag{2.18a}$$

$$V_n = -\mathrm{i}\alpha \sum_{m=-M}^{m=M} \sum_{j=0}^{j=K} m\left(w_{n-m}^j\right)_L G_j^m = 0, \quad M \geqslant n \geqslant 1. \tag{2.18b}$$

Relations required for evaluation of coefficients $(w_k^j)_L$, $(d_k^j)_L$ are given in Appendix A. The complex quantities F_n, $n = 0, 1, \ldots$ in (2.18) are the Fourier coefficients of the reference flow u_0 evaluated along the channel bottom, i.e.

$$u_0\left(y_L\left(x\right)\right) = \sum_{n=-\infty}^{n=\infty} (F_n)_L \, \mathrm{e}^{\mathrm{i}n\alpha x}. \tag{2.19}$$

In the present case, the non-zero Fourier coefficients have the form

$$(F_0)_L = -2S^2, \quad (F_1)_L = (F_{-1})_L = 2S, \quad (F_2)_L = (F_{-2})_L = -S^2 \tag{2.20}$$

Since no conditions can be written for V_0 (Szumbarski & Floryan 1999), equations (2.18) give $2M-1$ conditions for G_j^m.

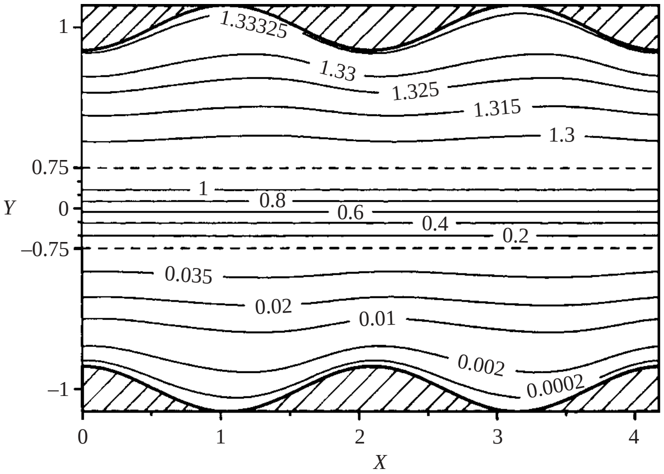

FIGURE 2. Streamlines of the flow in a diverging–converging channel subject to the fixed mass constraint for $Re = 1500$, $\alpha = 3$, $S = 0.02$ for two periods in the streamwise direction.

The condition required to specify the value of the streamfunction at the lower wall can be expressed as

$$\sum_{s=-M}^{s=M} \sum_{j=0}^{j=K} G_j^s \left(w_s^j\right)_L^* = -(H_0)_L, \tag{2.21}$$

where $(H_n)_L$ stands for the coefficients of Fourier expansion of the streamfunction Ψ_0 of the reference flow, i.e.

$$\Psi_0(y_L(x)) \approx \sum_{n=-M}^{n=M} (H_n)_L \mathrm{e}^{\mathrm{i}n\alpha x}. \tag{2.22}$$

Conditions at the upper wall can be expressed in a similar manner. Pressure condition (2.11) can be expressed at any value of y that does not cross the walls using standard procedures.

The system of nonlinear algebraic equations resulting from the discretization process is solved using an iterative method described by Szumbarski & Floryan (1999).

The method described above is very convenient for the analysis of the effect of variations of channel geometry as the changes in the form of the geometry are reduced to changes of the numerical values of Fourier coefficients only.

2.2. *Flow description*

Streamlines of the flow for parameter values of interest in this analysis, i.e. $Re = 1500$, $\alpha = 3$, $S = 0.02$, are displayed in figure 2. Nonlinear effects create a slight asymmetry of the flow on the upstream and downstream sides of the largest channel constriction. The flow is expected to separate on the downstream side for large enough constriction. Such separation did not occur for parameter values considered in this analysis.

The streamline pattern demonstrates that presence of channel divergence–convergence results in changes in the flow direction. The magnitude of these changes and the magnitude of the resulting centrifugal forces can be determined by studying the distribution of streamline curvature. The curvature K can be evaluated according

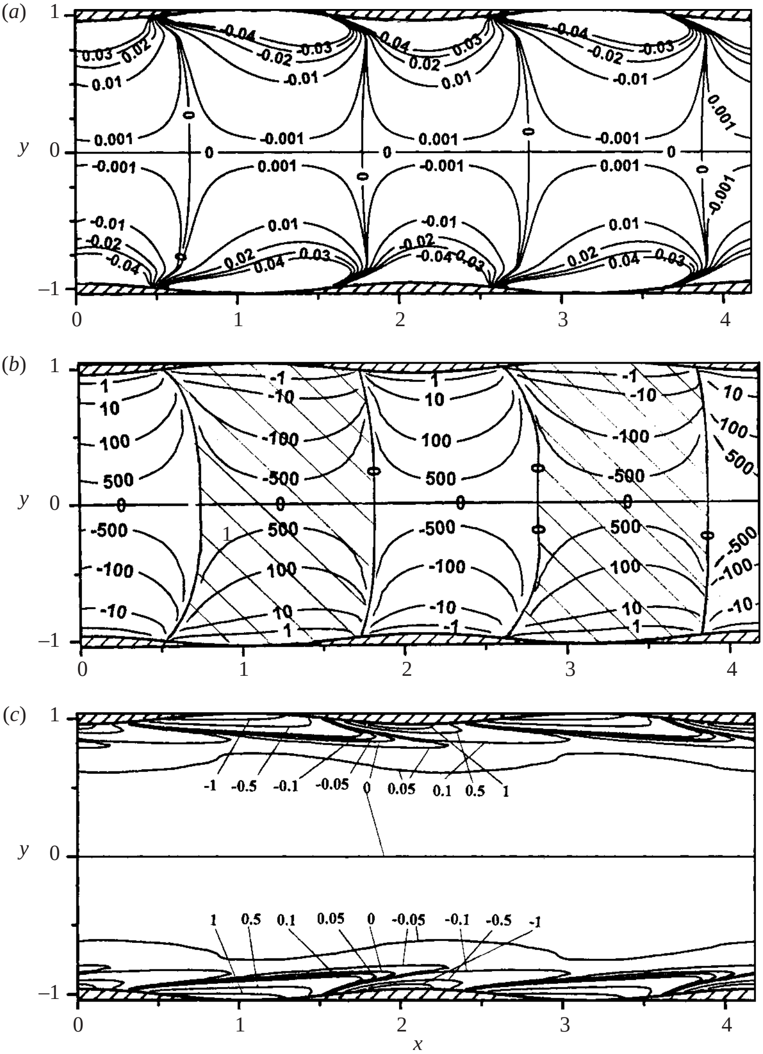

FIGURE 3. Properties of the flow in a diverging–converging channel for $Re = 1500$, $\alpha = 3$, $S = 0.02$. (a) Streamline curvature, (b) circulation, (c) additional vorticity associated with flow divergence–convergence (i.e. difference between the total vorticity and the vorticity of the Poiseuille flow). The shaded area denotes the sector in the flow field where the Rayleigh criterion is violated.

to the formula

$$K = \left(u_1^2 \frac{\partial v_1}{\partial x} - v_1^2 \frac{\partial u_1}{\partial y} - 2 v_1 u_1 \frac{\partial u_1}{\partial x} \right) \bigg/ \left(v_1^2 + u_1^2 \right)^{3/2}, \qquad (2.23)$$

and its distribution is illustrated in figure 3(a) for two periods in the streamwise direction. The curvature is negative in the lower half of the channel over approximately the first half period, and positive over the second half; the curvature is opposite in the upper half of the channel.

Potential for instability driven by the centrifugal effect is expressed in terms of the Rayleigh criterion (Rayleigh 1920; Drazin & Reid 1981) that states that a necessary and sufficient condition for stability is that the square of circulation should not decrease anywhere. This criterion had been derived in the case of flow between circular cylinders using a polar system of coordinates where the positive direction is uniquely defined. In the present case, the flow is described in terms of a Cartesian system and thus the positive direction corresponds to increasing y in the area where the curvature is negative, and decreasing y in the area where the curvature is positive. The circulation Γ can be evaluated according to the formula

$$\Gamma = (|\bar{v}|/K) = \left(v_1^2 + u_1^2\right)^2 \bigg/ \left(u_1^2 \frac{\partial v_1}{\partial x} - v_1^2 \frac{\partial u_1}{\partial y} - 2 v_1 u_1 \frac{\partial u_1}{\partial x}\right) \tag{2.24}$$

and its distribution is illustrated in figure 3(*b*). The shaded area denotes the flow sector where the Rayleigh criterion is violated. Figure 3(*c*) illustrates distribution of additional vorticity in the base flow that is created owing to the presence of the channel divergence–convergence. This additional vorticity is defined as the difference between the total vorticity and the vorticity associated with the Poiseuille flow.

3. Linear stability analysis

The analysis begins with the governing equations in the form of vorticity transport and continuity equations in the form

$$\frac{\partial \boldsymbol{\omega}}{\partial t} - (\boldsymbol{\omega} \cdot \nabla)\boldsymbol{v} + (\boldsymbol{v} \cdot \nabla)\boldsymbol{\omega} = \frac{1}{Re}\nabla^2 \boldsymbol{\omega}, \quad \nabla \cdot \boldsymbol{v} = 0, \quad \boldsymbol{\omega} = \nabla \times \boldsymbol{v}, \tag{3.1a–c}$$

and generalizes the analysis given by Floryan (1997). Unsteady, three-dimensional disturbances are superimposed on the mean part in the form

$$\boldsymbol{\omega} = \boldsymbol{\omega}_2(x, y) + \boldsymbol{\omega}_3(x, y, z, t), \quad \boldsymbol{v} = \boldsymbol{v}_2(x, y) + \boldsymbol{v}_3(x, y, z, t), \tag{3.2}$$

where subscripts 2 and 3 refer to the mean flow and the disturbance field, respectively. The assumed form, (3.2), of the flow is substituted into (3.1), the mean part is subtracted and the equations are linearized. The resulting linear disturbance equations have the form

$$\frac{\partial \boldsymbol{\omega}_3}{\partial t} + (\boldsymbol{v}_2 \cdot \nabla)\boldsymbol{\omega}_3 - (\boldsymbol{\omega}_3 \cdot \nabla)\boldsymbol{v}_2 + (\boldsymbol{v}_3 \cdot \nabla)\boldsymbol{\omega}_2 - (\boldsymbol{\omega}_2 \cdot \nabla)\boldsymbol{v}_3 = \frac{1}{Re}\nabla^2 \boldsymbol{\omega}_3, \tag{3.3a}$$

$$\nabla \cdot \boldsymbol{v}_3 = 0, \quad \boldsymbol{\omega}_3 = \nabla \times \boldsymbol{v}_3. \tag{3.3b,c}$$

The mean flow is assumed to have the form

$$\boldsymbol{v}_2(x, y) = [u_0(y), 0, 0] + \sum_{n=-\infty}^{n=\infty} \left[f_u^{(n)}(y),\ f_v^{(n)}(y),\ 0\right] \exp(\mathrm{i} n \alpha x), \tag{3.4}$$

where $f_u^{(n)}$, $f_v^{(n)}$ represent the solution to the problem (2.6)–(2.8) and $f_u^{(n)} = (f_u^{(-n)})^*$, $f_v^{(n)} = (f_v^{(-n)})^*$.

The disturbance equations, (3.3), have coefficients that are functions of x and y only and thus the solution can be written in the form

$$\boldsymbol{v}_3\,(x, y, z, t) = \boldsymbol{h}_3(x, y)\mathrm{e}^{\mathrm{i}(\mu z - \sigma t)} + \text{c.c.}, \tag{3.5a}$$

where

$$\boldsymbol{h}_3(x, y) = [h_u(x, y), h_v(x, y), \mathrm{i} h_w(x, y)]. \tag{3.5b}$$

Since our interest is in disturbances in the form of streamwise vortices, the x and y components of $\boldsymbol{h}_3$ are real, while the z-component is imaginary. The exponent μ is real and accounts for the spanwise periodicity of the vortices. The imaginary part of the exponent σ describes the rate of growth of the vortices. The exponent σ is purely imaginary in the case of stationary vortices. Only such vortices have been found in the present study.

Since the coefficients in (3.3) are periodic in x with periodicity $2\pi/\alpha$, $\boldsymbol{h}_3$ is written, following the Floquet theory (Coddington & Levinson 1965), as

$$\boldsymbol{h}_3(x, y) = \mathrm{e}^{\mathrm{i}\delta x}\boldsymbol{g}_3(x, y) = \mathrm{e}^{\mathrm{i}\delta x}\sum_{m=-\infty}^{m=+\infty} \boldsymbol{G}^{(m)}(y)\mathrm{e}^{\mathrm{i}m\alpha x}, \tag{3.6}$$

where $\boldsymbol{g}_3$ is periodic in x with the same periodicity $2\pi/\alpha$ and δ is referred to as the Floquet exponent. The Floquet exponent can be assumed to be $\delta = 0$ without loss of generality as the vortex disturbance must always retain a component that is constant in the x-direction. The final form of the disturbance velocity vector is written as

$$\boldsymbol{v}_3(x, y, z, t) = \sum_{m=-\infty}^{m=+\infty} \left[g_u^{(m)}(y), g_v^{(m)}(y), g_w^{(m)}(y)\right]\mathrm{e}^{\mathrm{i}(m\alpha x+\mu z-\sigma t)} + \text{c.c.}, \tag{3.7}$$

where $g_u^{(m)} = g_u^{(-m)^*}$, $g_v^{(m)} = g_v^{(-m)^*}$, $g_w^{(m)} = -g_w^{(-m)^*}$ and the asterisk denotes complex conjugate. Substitution of (3.4) and (3.7) into the disturbance equations, (3.3), and separation of Fourier components result in a system of ordinary differential equations governing $g_u^{(m)}$, $g_v^{(m)}$, $g_w^{(m)}$ in the form

$$\mathrm{S}^{(m)}\left(t_m g_w^{(m)} - \mu g_u^{(m)}\right) + \mathrm{C}g_v^{(m)} = \mathrm{i}Re\sum_{n=-\infty}^{n=\infty}\left(\mathrm{W}_u^{(m,n)}g_u^{(m-n)} + \mathrm{W}_v^{(m,n)}g_v^{(m-n)} + \mathrm{W}_w^{(m,n)}g_w^{(m-n)}\right), \tag{3.8a}$$

$$\mathrm{T}^{(m)}g_v^{(m)} = -Re\sum_{n=-\infty}^{n=\infty}\left(\mathrm{B}_u^{(m,n)}g_u^{(m-n)} + \mathrm{B}_v^{(m,n)}g_v^{(m-n)} + \mathrm{B}_w^{(m,n)}g_w^{(m-n)}\right), \tag{3.8b}$$

$$\mathrm{i}t_m g_u^{(m)} + \mathrm{D}g_v^{(m)} + \mathrm{i}\,\mu g_w^{(m)} = 0, \tag{3.8c}$$

where $t_m = m\alpha$ and the explicit forms of the operators T, S, C, W, B are given in Appendix B. Equation (3.8a) describes the y-component of disturbance vorticity, (3.8b) corresponds to $\mathrm{i}\mu \times (x$-component of vorticity$) - \mathrm{i}t_m \times (z$-component of vorticity$)$, and (3.8$c$) results from the continuity equation. It is convenient for analysis purposes to express the above relations in terms of the y-components of disturbance vorticity $\theta^{(m)} = t_m g_w^{(m)} - \mu g_u^{(m)}$ and disturbance velocity $g_v^{(m)}$, i.e.

$$\mathrm{S}^{(m)}\theta^{(m)} + \mathrm{C}g_v^{(m)} = Re\sum_{n=-\infty}^{n=\infty}\left(\mathrm{E}_v^{(m,n)}g_v^{(m-n)} + \mathrm{E}_\theta^{(m,n)}\theta^{(m-n)}\right), \tag{3.9a}$$

$$\mathrm{T}^{(m)}g_v^{(m)} = -Re\sum_{n=-\infty}^{n=\infty}\left(\mathrm{H}_v^{(m,n)}g_v^{(m-n)} + \mathrm{H}_\theta^{(m,n)}\theta^{(m-n)}\right) \tag{3.9b}$$

where the explicit forms of the operators E and H are given in Appendix B.

Equations (3.9) supplemented by homogeneous boundary conditions at $y = y_U(x)$ and $y = y_L(x)$ have non-trivial solutions only for certain combinations of parameters σ and μ. The required dispersion relation must be determined numerically. For the purposes of calculation, the problem is posed as an eigenvalue problem for σ.

Effects of channel divergence–convergence are contained in the terms on the right-hand side of (3.9) and in the boundary conditions. In the limit $\mathrm{S} \to 0$ (absence of channel divergence–convergence), the right-hand sides in (3.9) become zero, all modes in the Fourier series (3.7) decouple and (3.9) describes stationary modes of the classical three-dimensional instability (see Appendix C). The analytical solution describing the streamwise vortex ($m = 0$) is given in Appendix C. The coupling due to the channel divergence–convergence involves $2N + 1$ consecutive terms from the Fourier series, where N describes the actual length of the Fourier series in (3.4). In analogy to stability of flow in a straight channel, we shall refer to the T, S and C operators as the Tollmien–Schlichting, Squire and coupling operators, respectively. Operators E and H arise because of the presence of channel divergence–convergence. Since the wall corrugation can be viewed as flow forcing, we shall refer to these operators as the forcing operators. E_θ and H_v describe direct forcing and E_v and H_θ describe coupling due to the forcing.

The boundary conditions at the walls represent another set of coupling and forcing operators arising because of the presence of channel divergence–convergence. Although the form of these operators cannot be given explicitly in general, it is possible to construct an explicit form of the equivalent linear algebraic operators resulting from the numerical discretization procedure. This process is described in the next section.

3.1. *Numerical solution*

The problem to be solved consists of an infinite system of ordinary differential equations, (3.9), with homogeneous boundary conditions. Approximate solutions can be found by truncating the sum in (3.7) after a finite number L of terms and solving the eigenvalue problem for $L + 1$ differential equations of type (3.9).

The differential equations were discretized using a method similar to that described in § 2.1. Boundary conditions at the upper an lower walls were implemented using the immersed boundary conditions concept described in § 2.1. The discretization procedure results in a matrix eigenvalue problem $\Omega x = 0$ where $\Omega(\sigma)$ represents the coefficient matrix. This matrix is linear in σ, i.e. $\Omega = \Omega_0 + \Omega_1 \sigma$, where $\Omega_0 = \Omega(0)$, $\Omega_1 = \Omega(1) - \Omega_0$. The σ-spectrum is determined by solving a general eigenvalue problem in the form $\Omega_0 x = \sigma \Omega_1 x$. The individual eigenvalues are determined by finding zeros of the determinant of Ω.

Two methods for the tracing of eigenvalues in the parameter space have been used. In the first method, we alter flow conditions and produce an approximation for the eigenvalue which is then improved iteratively by searching for the near-by zero of the determinant using a Newton–Raphson search procedure. In the second method, the inverse iterations method, we compute an approximation for the eigenvector Λ_a corresponding to the unknown eigenvalue σ_a using an iterative process in the form $(\Omega_0 - \sigma_0 \Omega_1)\Lambda^{(n+1)} = \Omega_1 \Lambda^{(n)}$ where σ_0 and $\Lambda^{(0)}$ are the eigenvalue and the eigenvector (an eigenpair) corresponding to the unaltered flow. If σ_a is the eigenvalue closest to σ_0, $\Lambda^{(n)}$ converges to Λ_a. The eigenvalue σ_a is evaluated using formula $\sigma_a = \Lambda_a^* \Omega_0 \Lambda_a / \Lambda_a^* \Omega_1 \Lambda_a$ where asterisk denotes the complex conjugate transpose. The inverse iterations method was found to be generally more efficient.

Results of numerical tests presented in table 1 assist in identifying the correct values of various numerical parameters to be used in the computations. The eigenvalues can be determined with accuracy no worse then three digits using $K = 59$ Chebyshev polynomials, $M = 5$ Fourier modes to represent the mean flow and $L = 5$ Fourier modes to represent the disturbances.

(*a*)

Number of Fourier modes used to represent disturbances	Number of mean flow Fourier modes retained in the stability equations	Number of Fourier modes used in the mean flow solution		
		3	5	7
3	3	0.173433	0.169721	0.169552
5	3	0.171937	0.168074	0.167918
	5		0.168147	0.167980
7	3	0.171984	0.168132	0.167974
	5		0.168151	0.167982
	7			0.167984

(*b*)

Number of Chebyshev polynomials	39	49	59	69	79
$\mathrm{Im}(\sigma) \times 10^3$	0.167942	0.167963	0.167983	0.167984	0.167984

TABLE 1. Disturbance amplification rate (*a*) $\mathrm{Im}(\sigma) \times 10^3$, (*b*) $\mathrm{Im}(\sigma)$ for the corrugation amplitude $S = 0.02$, the corrugation wavenumber $\alpha = 3$, the flow Reynolds number $Re = 1500$, the vortex wavenumber $\mu = 2$, the first instability mode and the flow subject to the fixed mass constraint obtained using (*a*) $K = 79$ Chebyshev polynomials and (*b*) $M = L = 7$ Fourier modes to represent the mean flow and the disturbance field.

4. Discussion of results

It is convenient to begin discussion with a brief summary of stability properties of flow in a straight channel. Such flow becomes unstable with respect to two-dimensional waves (Tollmien–Schlichting waves) travelling in the downstream direction at the flow Reynolds number $Re = 5772$. The instability has a subcritical character and an increase of the level of disturbances can reduce the critical Reynolds number down to $Re \approx 2700$ (Herbert 1977). Stable, two-dimensional waves of sufficient amplitude can produce three-dimensional instability that can give rise to streamwise vortices at Re as low as 1000 (Orszag & Patera 1983); this process is referred to as secondary instability and is attributed to parametric resonance.

The flow in a diverging–converging channel is expected to be subject to the travelling wave instability. The change of the corresponding critical Reynolds number as a function of the channel geometry is yet to be studied. The same flow can also be subject to an instability driven by the centrifugal effects that, under certain conditions, may give rise to the amplification of disturbances in the form of streamwise vortices. The present analysis is focused on the centrifugal effect. The flows of interest are characterized by rather small Reynolds numbers where the travelling waves are expected to be linearly stable or, at least, the centrifugal instability is expected to be dominant.

The form of the flow in a diverging–converging channel and its stability characteristics depend on whether the flow is allowed to develop with the same mass flux as the reference flow in a straight channel, or whether it is driven by the same pressure gradient. The following discussion deals with the case of a flow with a fixed mass flux unless explicitly noted otherwise.

The instability that results in the formation of streamwise vortices occurs for sufficiently high Reynolds numbers if the channel geometry satisfies certain conditions. This analysis has been carried out in the context of a reference diverging–converging channel whose walls are described by the sine functions, with the amplitude S and the wavelength $\alpha/2\pi$ being the only geometric parameters. The vortices that are

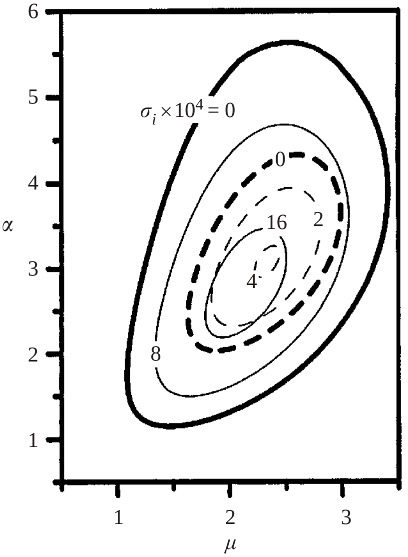

FIGURE 4. Amplification rates $\mathrm{Im}(\sigma)$ of disturbances in the form of streamwise vortices induced in a flow with Reynolds number $Re = 1500$ subject to the fixed mass flux constraint as a function of the wall wavenumber α and the vortex wavenumber μ for the amplitude of the channel divergence–convergence $S = 0.02$. ——, First, and – – –, second instability mode.

amplified are fixed with respect to the wall, i.e. $\mathrm{Re}(\sigma) = 0$, and are modulated in the streamwise direction with the same periodicity as the channel, i.e. the wavelength of the modulation is $\alpha/2\pi$. Two modes of the instability have been identified for the range of flow Reynolds numbers considered. The amplification rates $\mathrm{Im}(\sigma)$ for both modes are illustrated in figure 4 for the flow Reynolds number $Re = 1500$ and the amplitude of the channel divergence–convergence $S = 0.02$. The more unstable mode will be referred to as the first mode. It can be seen that the range of the active wall wavenumbers for the first mode extends from $\alpha \approx 1$ to $\alpha \approx 5.5$. The term 'active' refers here to the wall wavenumbers that give rise to the instability at this particular value of the flow Reynolds number and the wall amplitude. Each active wall wavenumber gives rise to a band of vortices whose wavelength is bounded from above and below. The amplified vortex wavenumbers corresponding to the first mode are always contained in the interval $\sim 1 < \mu < \sim 3.5$ at this particular value of Re (see figure 4), but the vortices that are actually amplified are contained in a smaller subinterval whose length and location change as a function of the wall wavenumber. The second mode is more stable in the sense that the range of the active wall wavenumbers is smaller, the band of the resulting vortices is narrower and the amplifications rates are smaller as compared to those corresponding to the first mode. It will be shown later in the discussion that this mode is associated with the disturbance velocity field characterized by higher velocity gradients; the associated higher dissipation

---

FIGURE 5. Eigenfunctions $g_u^{(m)}$, $g_v^{(m)}$, $g_w^{(m)}$, $m = 0, 1, 2$, describing vortex corresponding to the first instability mode with the wavenumber $\mu = 2$ induced by the channel divergence–convergence with the wall wavenumber $\alpha = 3$ and the amplitude $S = 0.02$ for the flow Reynolds number $Re = 1500$ and normalized with condition $\max_{y \in (0, 1+2S)}(g_u^{(0)}) = 1$. (*a*) $g_u^{(m)}$, (*b*) $g_v^{(m)}$, (*c*) $g_w^{(m)}$. The flow is subject to the fixed mass constraint. Subscripts r and i denote real and imaginary parts.

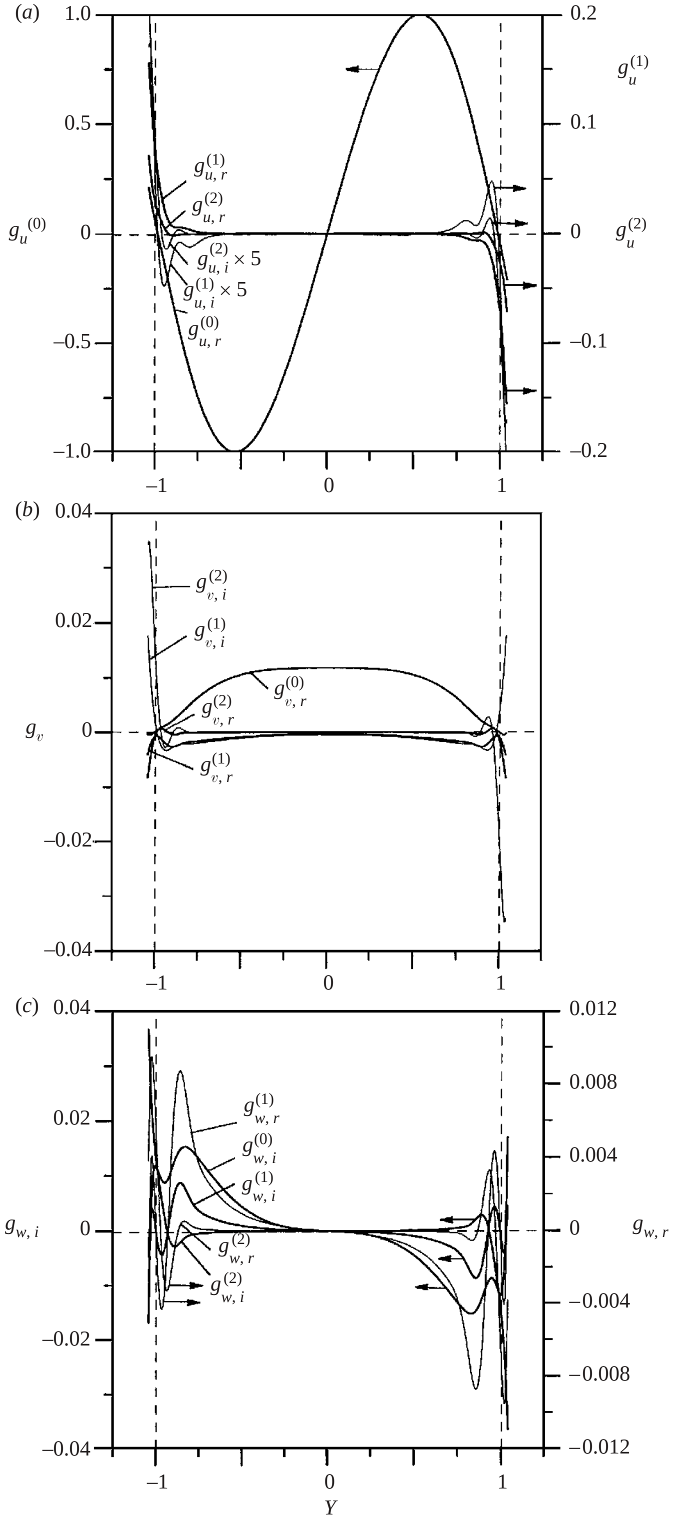

FIGURE 5. See facing page for caption.

is responsible for the relative stabilization of this mode. We shall now discuss properties of both modes as they result in qualitatively different disturbance velocity fields.

Figure 5 illustrates the first three eigenfunctions corresponding to the first mode of the instability. The dominant character of $g_u^{(0)}$, which is a characteristic feature of the vortices, is clearly visible. Because $g_u^{(0)}$ is antisymmetric, we could refer to this mode as antisymmetric. The shape of $g_v^{(0)}$ (figure 5*b*) suggests existence of single layer of vortices occupying most of the channel opening. The eigenfunctions shown are normalized with the maximum of $g_u^{(0)}$ in the upper half of the channel, i.e. $\max_{y\in(0,1+2S)}(g_u^{(0)})=1$. Note that, because of symmetries, the maximum of $g_u^{(0)}$ in the upper half of the channel is equal to the minimum of $g_u^{(0)}$ in the lower half. Use of the maximum of $g_u^{(0)}$ in the lower half for normalization purposes would result in the vortices displayed rotating in the opposite direction.

The topology of the disturbance velocity field is complex and is illustrated in figure 6 using the velocity 'amplitude function' $\boldsymbol{h}_3(x, y)$ (see (3.5)). Whereas most of the channel is 'filled in' with a single layer of vortices, there are thin layers attached to each of the walls where a significant flow readjustment in the streamwise direction takes place, as indicated by the zero of the normal- and spanwise-velocity-component 'amplitude functions' h_v and h_w (figure 6*b*, *c*). The streamwise changes in the structure of the disturbance velocity field are illustrated in figure 7 which displays spanwise cuts through the disturbance velocity field starting at $x=0$ every $1/8\lambda$, where $\lambda = 2\pi/\alpha$ denotes the length of the period. The vertical extent of the central vortex changes with channel opening; the vortex appears to be 'round' where the channel is narrowest (figure 7*a*) becomes elongated in the vertical direction as the channel diverges (figure 7*b*–*d*) and returns to its original 'round' shape as the channel converges (figure 7*e*–*h*). The size of the vortex appears to be dictated indirectly by the size of channel opening through the changes in the thickness of the readjustment layers at both walls.

The inner structure of the readjustment layers is illustrated in figure 8, which displays enlargement of the flow shown in figure 7 in the area near the upper wall. There are qualitative differences in the form of these layers in the diverging and converging sections of the channel, with a complex evolution in the diverging section and a rather simple form in the converging section. We shall start this discussion with the diverging section using the nomenclature of the critical point theory (Perry & Fairlie 1974). Note the existence of a second vortex near the wall at $x=0$ (figure 8*a*). The thickness of the layer where the flow moves in the direction opposite to that dictated by the central vortex increases as channel diverges (figure 8*b*) with the second vortex disappearing and being replaced by a saddle. This process continues at $x=\frac{1}{4}\lambda$ (figure 8*c*) and $x=\frac{3}{8}\lambda$ (figure 8*d*). At $x=\frac{1}{2}\lambda$ (largest channel opening) the flow near the wall changes direction, resulting in the formation of another secondary vortex above the saddle (figure 8*e*). The secondary vortex and the saddle disappear at $x=\frac{5}{8}\lambda$ (figure 8*f*) and the structure of the flow remains approximately unchanged further downstream at $x=\frac{3}{4}\lambda$ and $x=\frac{7}{8}\lambda$ (figure 8*g*, *h*).

The differences between the diverging and converging sections of the channel are shown in figure 9 which displays a modified disturbance velocity field in the (x, y)-plane at $z=0$. The modification involves elimination of the zero mode from the u velocity component, i.e. elimination of $g_u^{(0)}$. This component is by an order of magnitude larger then others (see figure 5) and thus conceals streamwise modulation of the disturbance velocity field. The flow modulation has a simple form. As the

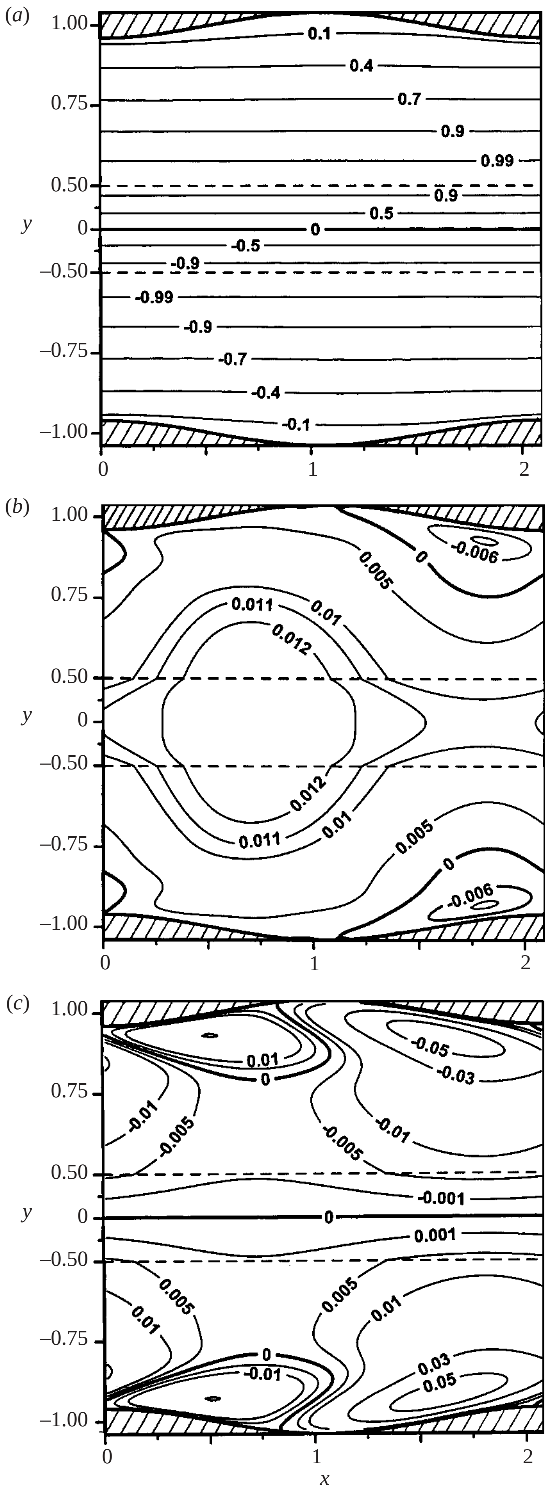

FIGURE 6. Velocity 'amplitude function' $\boldsymbol{h}_3(x, y) = [h_u(x, y), h_v(x, y), \mathrm{i}h_w(x, y)]$ (see equation (3.5)) corresponding to the first instability mode for $Re = 1500$, $\alpha = 3$, $\mu = 2$, $S = 0.02$ normalized with condition $\max_{y\in(0,1+2S)}(g_u^{(0)}) = 1$. (*a*) h_u, (*b*) h_v, (*c*) h_w. The flow is subject to the fixed mass constraint.

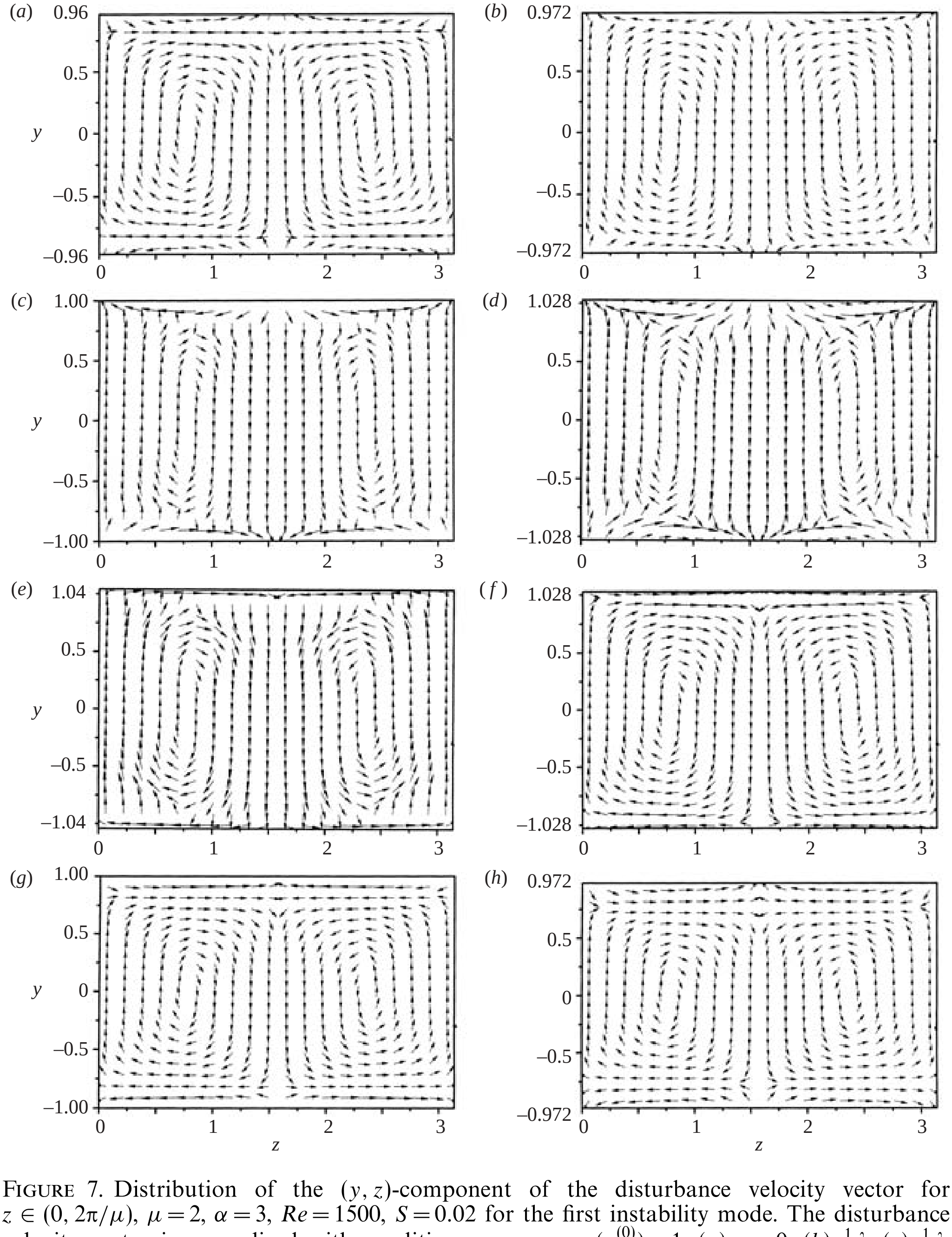

FIGURE 7. Distribution of the (y, z)-component of the disturbance velocity vector for $z \in (0, 2\pi/\mu)$, $\mu = 2$, $\alpha = 3$, $Re = 1500$, $S = 0.02$ for the first instability mode. The disturbance velocity vector is normalized with condition $\max_{y \in (0,1+2S)}(g_u^{(0)}) = 1$. (*a*) $x = 0$, (*b*) $\frac{1}{8}\lambda$, (*c*) $\frac{1}{4}\lambda$, (*d*) $\frac{3}{8}\lambda$, (*e*) $\frac{1}{2}\lambda$, (*f*) $\frac{5}{8}\lambda$, (*g*) $\frac{3}{4}\lambda$, (*h*) $\frac{7}{8}\lambda$, where $\lambda = 2\pi/\alpha$ denotes one wavelength of the wall divergence–convergence.

mean flow approaches the converging section, it is forced to change direction owing to the blocking effect of the wall; the resulting instability drives the flow in the spanwise direction resulting in the formation of a stable node (sink) close to the upper wall and an unstable node (source) close to the lower wall. This structure of

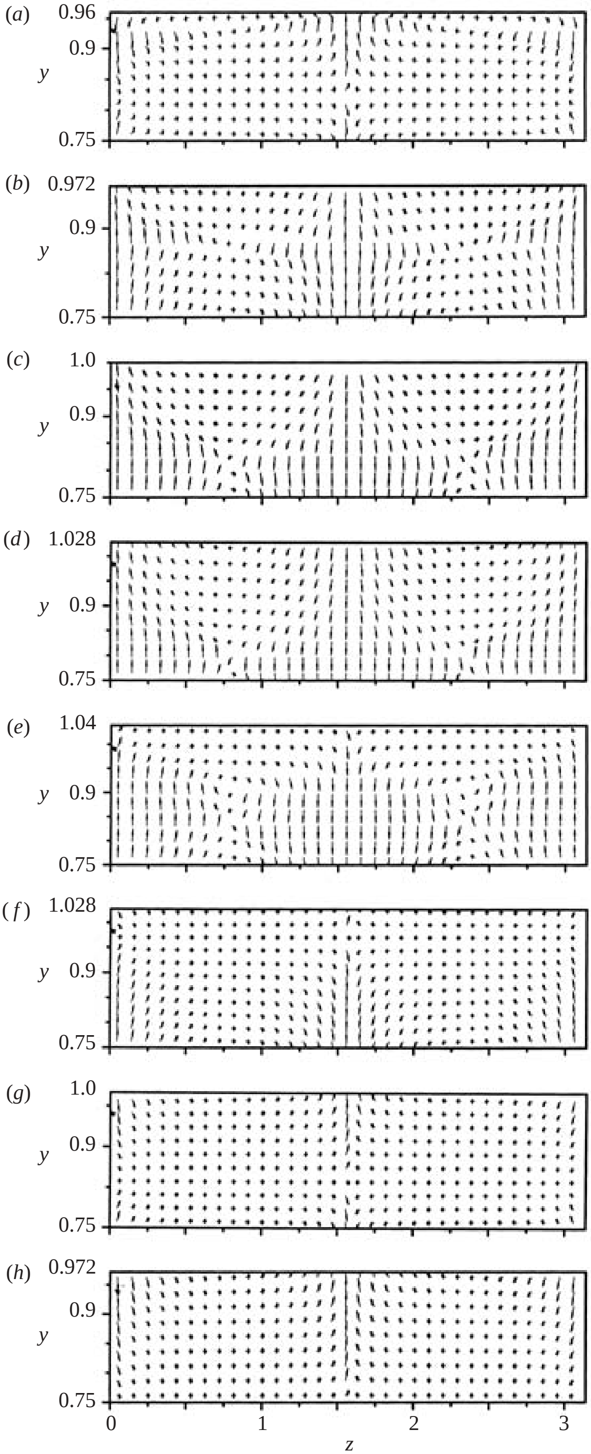

FIGURE 8. Enlargement of the segment of the disturbance velocity field near the upper wall corresponding to $y \in (0.75, 1 + 2S)$. The complete flow field is shown in figure 7.

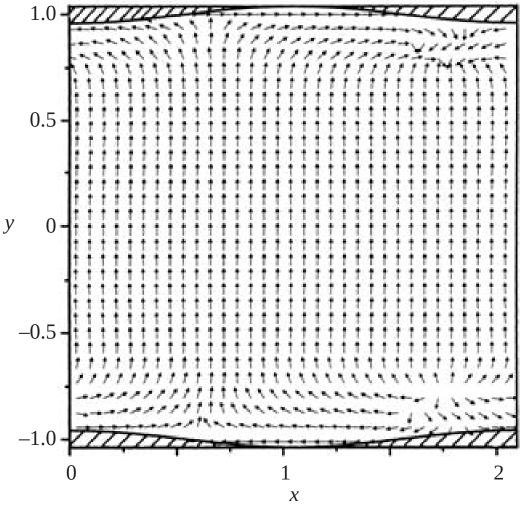

FIGURE 9. Distribution of the (x, y)-component of the modified disturbance velocity vector for $x \in (0, 2\pi/\alpha)$ at $z = 0$ for the first instability mode. The remaining conditions are the same as in figure 7. The modification involves elimination of the zero mode from the u velocity component, i.e. elimination of $g_u^{(0)}$.

the disturbance velocity field points towards the centrifugal-effect-driven origin of the instability.

The topology of the velocity disturbance field associated with the second mode is somewhat different. Figure 10 illustrates the first three eigenfunctions. The dominant character of $g_u^{(0)}$ is clearly visible. Because $g_u^{(0)}$ is symmetric, we could refer to this mode as symmetric. The shape of $g_v^{(0)}$ (figure 10*b*) suggests the existence of two layers of vortices in the central section of the channel cross-section. The eigenfunctions shown are normalized with the maximum of $g_u^{(0)}$ in the upper half of the channel, i.e. $\max_{y\in(0,1+2S)}(g_u^{(0)}) = 1$. Because of symmetries, the maximum of $g_u^{(0)}$ in the upper half is equal to the maximum of $g_u^{(0)}$ in the lower half and thus use of any of them for normalization purposes does not effect the direction of rotation of the vortices shown.

The topology of the disturbance velocity field associated with the second mode is illustrated in figure 11 using the velocity 'amplitude function' $\boldsymbol{h}_3(x, y)$ (see (3.5)). The channel is 'filled in' with two layers of vortices and thin readjustment layers attached to each of the walls (figure 11*b*,*c*). The streamwise changes in the structure of the disturbance velocity field are illustrated in figure 12 which displays spanwise cuts through the disturbance velocity field starting at $x = 0$ every $1/8\lambda$. The vertical extent of the central vortices changes with channel opening; their size is dictated indirectly by the size of channel opening through the changes in the thickness of the readjustment layers at both walls, as in the case of the first mode discussed earlier. There are qualitative differences in the form of the 'adjustments' layers in the diverging and converging sections of the channel, with a complex evolution in the diverging section (see figure 12*b*–*d*) and a rather simple form in the converging section (see figure 12*f*–*h*). The central vortices appear to almost disappear at $x = 3\lambda/8$ (figure 12*d*). Figure 13 displays a modified disturbance velocity field (i.e. without $g_u^{(0)}$) in the (x,y)-plane at $z = 0$. It can be seen that the streamwise modulation of the disturbance velocity field results in the formation of stable nodes (sinks) close to the

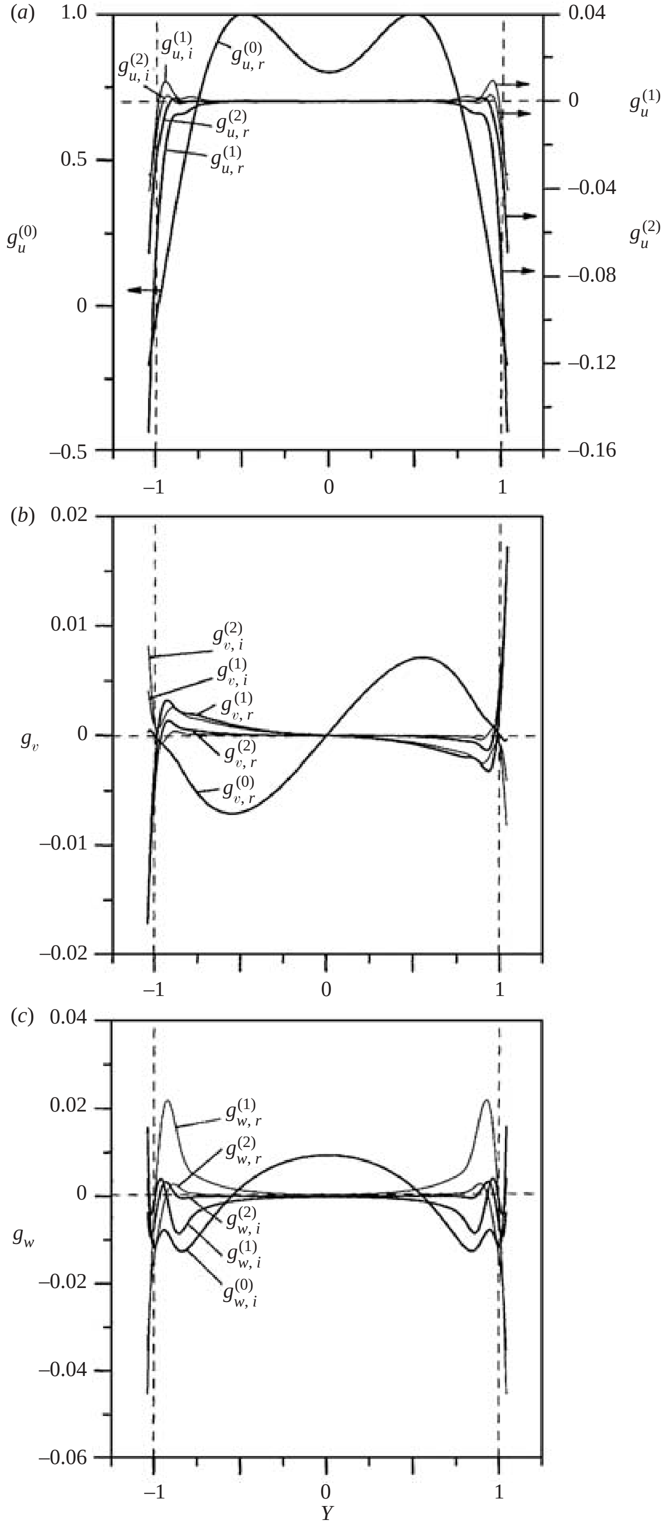

FIGURE 10. Eigenfunctions $g_u^{(m)}$, $g_v^{(m)}$, $g_w^{(m)}$, $m = 0$, 1, 2, corresponding to the second instability mode. The remaining conditions are as in figure 5.

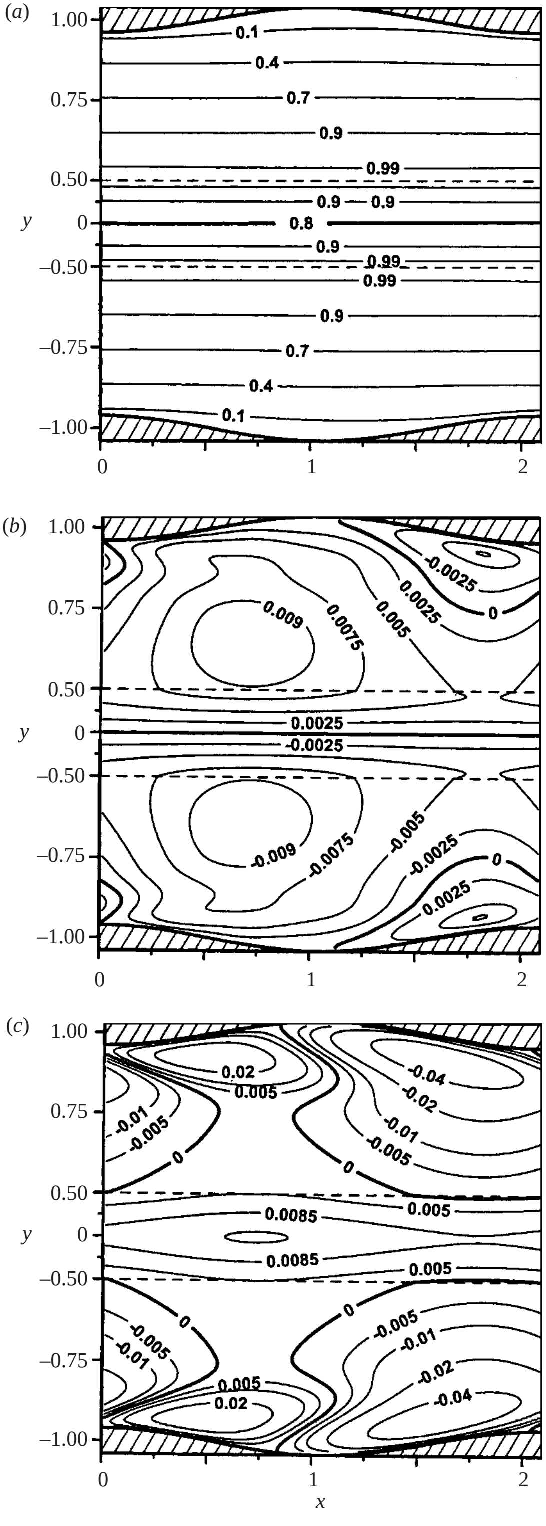

FIGURE 11. Velocity ‘amplitude function’ $\boldsymbol{h}_3(x, y) = [h_u(x, y), h_v(x, y), \mathrm{i}h_w(x, y)]$ (see equation (3.5)) corresponding to the second instability mode. The remaining conditions are as in figure 5.

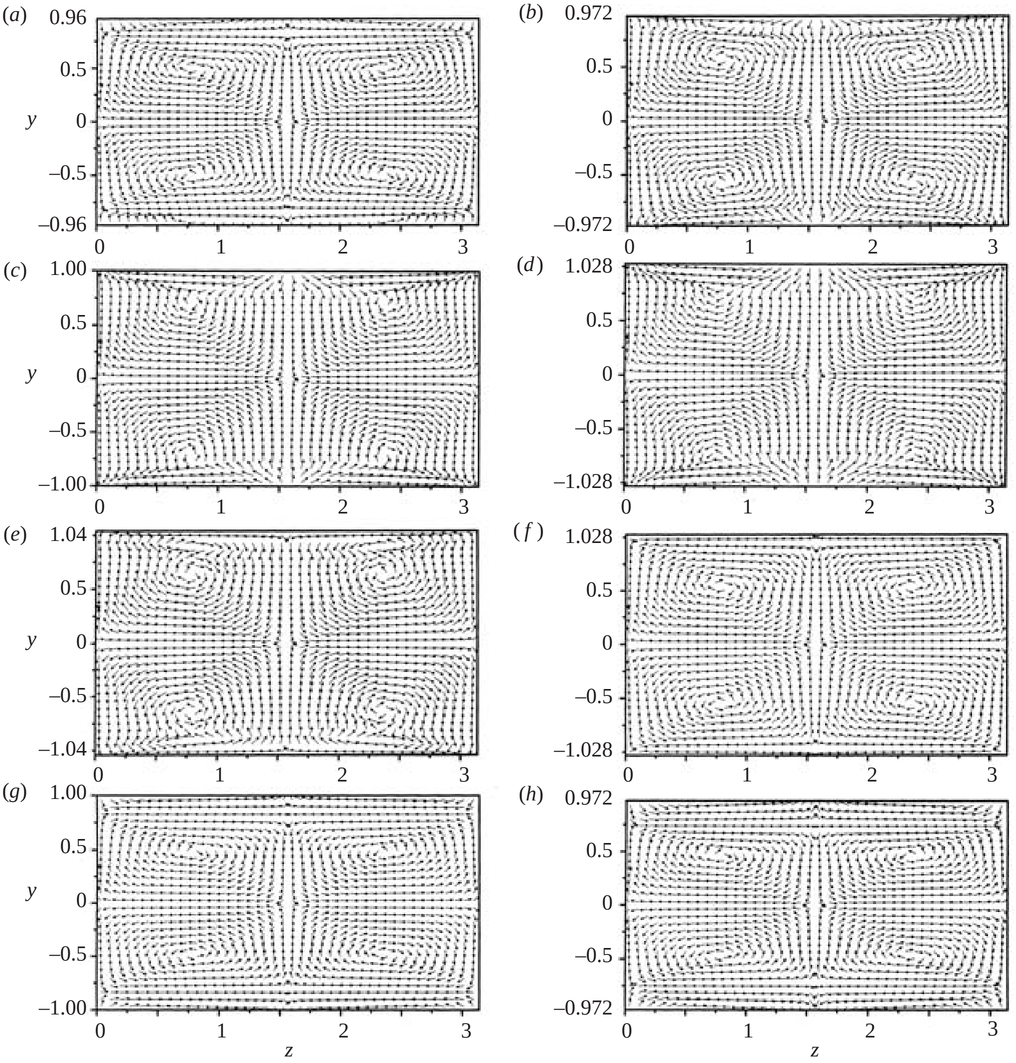

FIGURE 12. Distribution of the (y, z)-component of the disturbance velocity vector for $z \in (0, 2\pi/\mu)$, $\mu = 2$, $\alpha = 3$, $Re = 1500$, $S = 0.02$ for the second instability mode. The remaining conditions are as in figure 7.

upper and lower walls, although the structure of the velocity field in the immediate neighbourhood of these nodes is more complex than in the case of the first mode. These nodes are located in the converging section of the channel.

Figure 14 illustrates changes of the vortex amplification rate as a function of the amplitude S of the channel divergence–convergence for both instability modes in the limit as $S \rightarrow 0$. This limit permits identification of additional differences between both modes. The distinct limit $S = 0$ for the first mode corresponds to the Squire mode and can be determined analytically, i.e. $\sigma = -\mathrm{i}(\mu^2 + \frac{1}{4}\pi^2)/Re$ (see Appendix C). The same limit for the second mode corresponds to the Tollmien–Schlichting mode and can also be determined analytically, i.e. $\sigma = -\mathrm{i}(s^2 + \mu^2)/Re$ where s stands for the smallest positive root of $s\,\sin(s)\cosh(\mu) + \mu\,\sinh(\mu)\cos(s) = 0$ (see Appendix C). These results demonstrate that the first instability mode is connected to the Squire

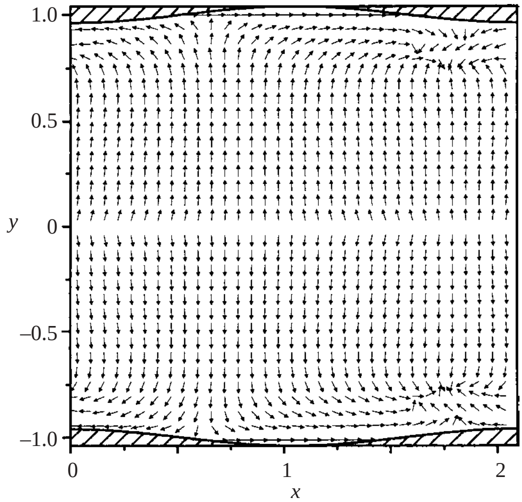

FIGURE 13. Distribution of the (x, y)-component of the modified disturbance velocity vector for $x \in (0, 2\pi/\alpha)$ at $z = 0$ for the second instability mode. The remaining conditions are the same as in figure 9.

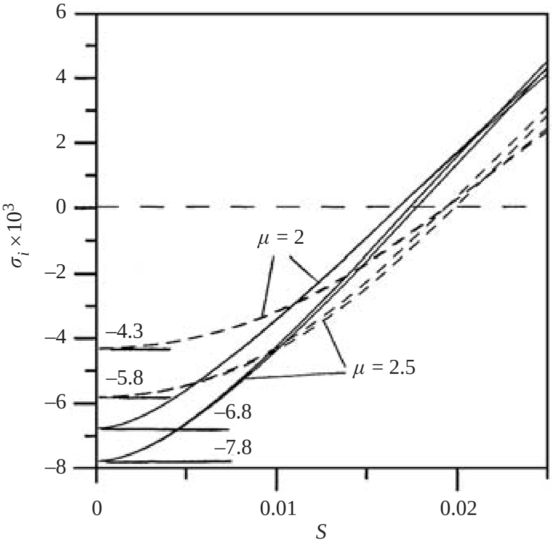

FIGURE 14. Variations of the amplification rate Imag(σ) of the streamwise vortices with the wavenumber $\mu = 2$ and $\mu = 2.5$ induced by the channel divergence–convergence with the wavenumbers $\alpha = 2.5$ and $\alpha = 3$ for $Re = 1500$ as a function of the amplitude S of the channel divergence–convergence. ——, First, and – – –, second instability modes. The wavenumber α is not marked, as it does not affect the limit of $S \to 0$ (see Appendix C). The flow is subject to the fixed mass constraint.

spectrum in the case of a smooth channel and the second mode is connected to the Tollmien–Schlichting spectrum.

Evolution of the $g_u^{(0)}$, $g_v^{(0)}$, $g_w^{(0)}$ eigenfunctions for both instability modes as a function of the amplitude S is illustrated in figure 15. Note that disturbances corresponding to the first mode have no streamwise vorticity when $S = 0$ (see Appendix C). Such vorticity may be viewed as being created by 'bending' of the plane vortex sheets by the channel divergence–convergence. The relevant mechanism is known as the CL1 mechanism (Leibovich 1983) and was described originally by Craik & Leibovich (1976) in the context of Langmuir circulation. Since both modes are driven by the same mechanism, the CL1 mechanism is not likely to play a major role in the current instability, but can certainly contribute to it.

Figure 16 displays the neutral surfaces in the (α, μ, S) space for $Re = 1500$ corresponding to both instability modes. The interiors of these surfaces correspond to the unstable flow conditions. The first mode is always more unstable, as expected, although the second mode can be induced with a correct combination of initial conditions. There is a range of parameters where only the first mode becomes unstable. The shapes of the neutral surfaces show that the range of the active wall wavenumbers α as well as the range of the resulting unstable vortex wavenumbers μ increase rapidly with an increase of the amplitude S of the channel divergence–convergence. Similar results obtained for $Re = 5000$ and displayed in figure 17 demonstrate that this increase is more rapid for higher values of Re, where it results in much wider ranges of active α and resulting μ. It can also be seen that the instability occurs at much smaller amplitudes S when Re is higher.

Figure 18 displays the neutral surfaces in the (α, μ, Re) space for $S = 0.008$. A rapid increase of the range of the active wall wavenumbers α and the resulting vortex wavenumbers μ as Re increases is clearly visible.

The present linear analysis is focused on the determination of the critical stability conditions only however, it is useful to comment on the expected subsequent evolution of the flow. One route of inquiry is the nonlinear evolution of the vortices; weak nonlinear effects could either enhance or suppress the instability. The second route is associated with the fact that the presence of the vortices leads to a significant rearrangement and rapid three-dimensionalization of the flow. Uplifting of low momentum fluid away from the wall leads to the formation of highly distorted streamwise and spanwise velocity profiles that are subject to very strong secondary instabilities. Correct modelling of this rearrangement requires inclusion of complete nonlinear effects (Benmalek & Saric 1994). The experimental evidence available in the case of Görtler instability (Floryan 1991) suggests that the flow is likely to follow the latter route and, indeed, the secondary instabilities are expected to have the form similar to that found in the case of Görtler vortices. Additional complications may arise owing to the presence of the readjustment layers at both walls, which give rise to another class of strong shear layers. These layers may induce secondary instabilities not associated with those driven by the central vortices. This discussion suggests that the flow evolution past the critical conditions is likely to require fully nonlinear analysis, with weakly nonlinear models probably unable to capture its salient features.

Since the presence of vortices is a strong harbinger of transition to turbulence, we are interested in determining the characteristics of the channel geometry and the critical flow conditions that lead to the onset of the instability. Channel geometry considered here is completely defined in terms of the amplitude S and wavelength $\alpha/2\pi$ of the divergence–convergence pattern. The critical Reynolds number defining the onset of the instability can be found for each combination of these two parameters. A cut corresponding to $\alpha = \text{const}$ through the neutral surface shown in figure 18 defines such Reynolds number for this particular α and $S = 0.008$. A similar cut through the neutral surface shown in figure 16 determines the amplitude S for which $Re = 1500$ represents the critical value. It is convenient for presentation of the results to introduce the global critical Reynolds number $Re_{g,cr}$ that defines the critical conditions for the

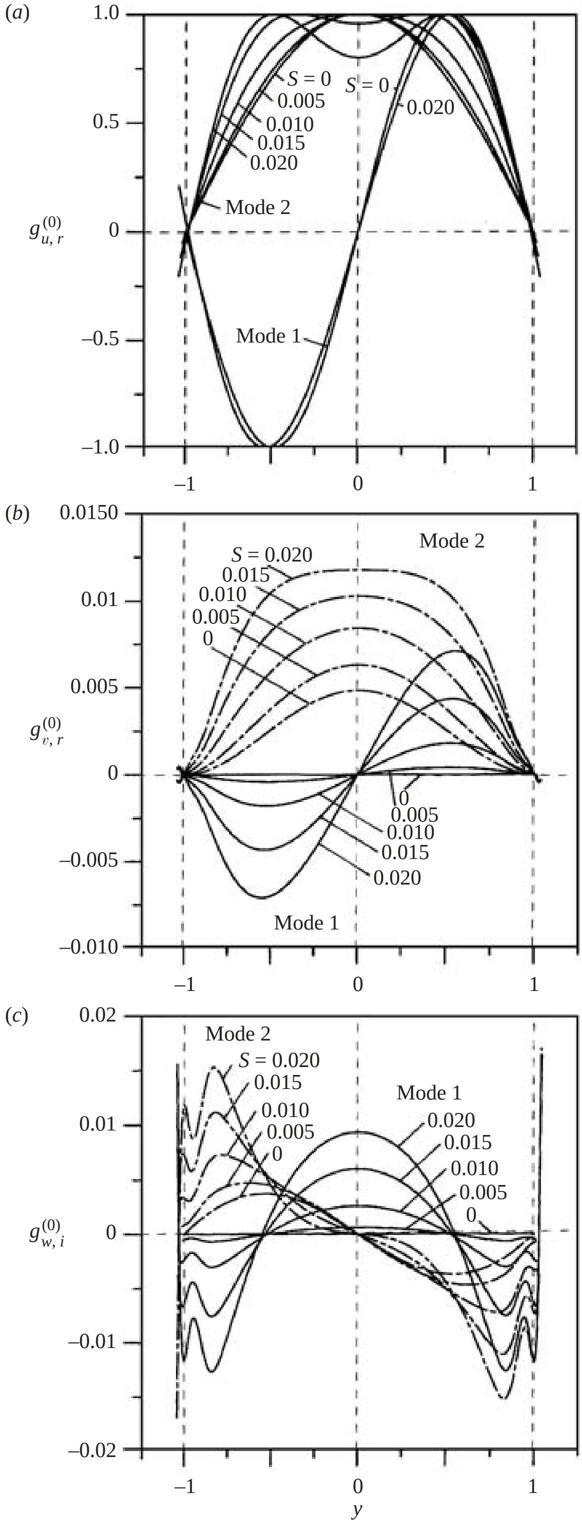

FIGURE 15. See facing page for caption.

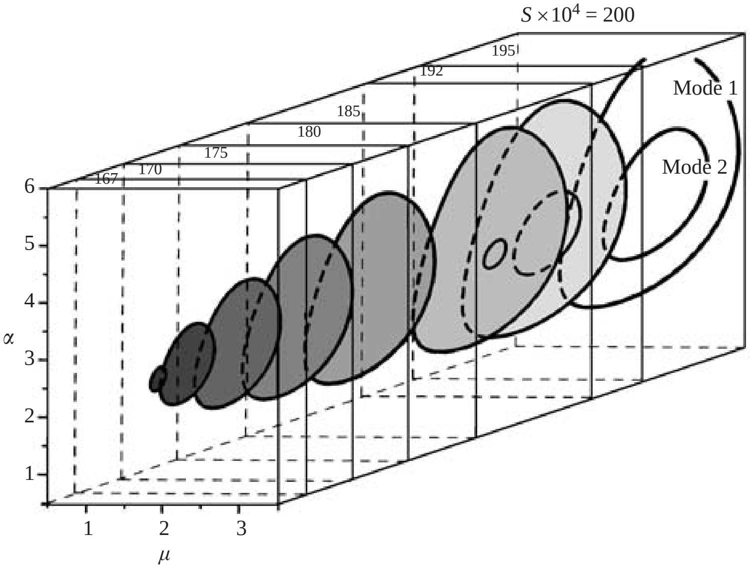

FIGURE 16. The neutral surfaces describing variation of the neutral stability conditions for the first and second instability modes for the Reynolds number $Re = 1500$ as a function of the amplitude S and the wavenumber α of the channel divergence–convergence, and the vortex wavenumber μ. The flow is subject to the fixed mass constraint.

onset of the instability for a given amplitude S of the wall divergence–convergence regardless of its wavelength. Such global critical conditions, which include the critical wavelength of the channel geometry $\alpha_{g,cr}$ and the critical wavelength of the resulting vortex $\mu_{g,cr}$, correspond to the tip of the neutral surface shown in figure 18. Variations of the global critical conditions as a function of the channel divergence–convergence amplitude S are illustrated in figure 19 for both instability modes. The values of $Re_{g,cr}$ for the first mode are $Re_{g,cr}$ = 56120, 6697, 2788, 1211 at S = 0.001, 0.005, 0.01, 0.02, respectively. The values of $Re_{g,cr}$ can be expressed using simple correlation in the form

$$\ln(Re_{\boldsymbol{g},cr}) = -1.2796\ln(S) + 2.048 \tag{4.1}$$

which provides accuracy no worse then 5% for $S < 0.02$.

The area below the critical curves in figure 19 defines the range of the amplitudes S and the flow Reynolds numbers Re under which the flow is stable. The first mode determines the critical stability conditions, although the second mode can be induced with a correct selection of the initial conditions if the Reynolds number is high enough. It is worth noting that the critical wall wavenumber for the second mode is almost twice as large as for the first mode whereas the wavenumbers of the resulting vortices are very similar.

The results presented so far have dealt with the stability of a flow that developed under the fixed mass flux constraint. Note that such flow is associated with a pressure

---

FIGURE 15. Evolution of the eigenfunctions (a) $g_u^{(0)}$, (b) $g_v^{(0)}$, (c) $g_w^{(0)}$, corresponding to the first and second instability modes as a function of the amplitude S of the channel divergence–convergence for the wall wavenumber $\alpha = 3$, the vortex wavenumber $\mu = 2$, and the flow Reynolds number $Re = 1500$. Normalization condition $\max_{y\in(0,1+2S)}(g_u^{(0)}) = 1$. The flow is subject to the fixed mass constraint. Subscripts r and i denote real and imaginary parts.

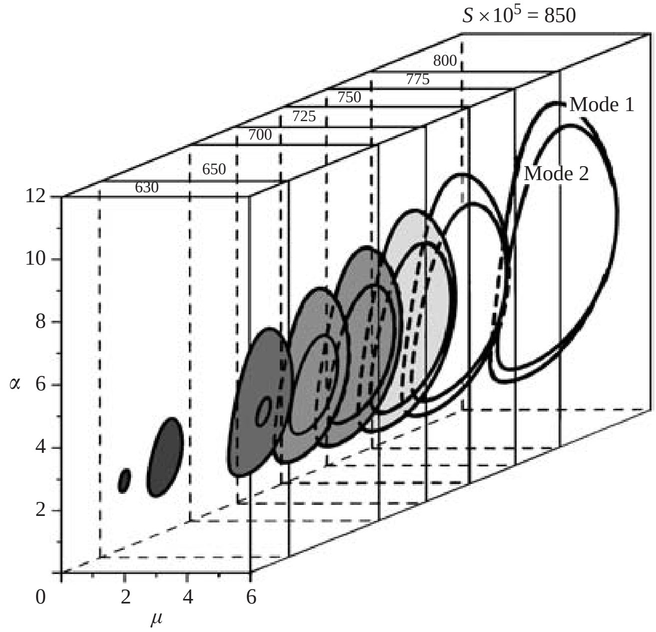

FIGURE 17. The same as in figure 16, but with the Reynolds number $Re = 5000$.

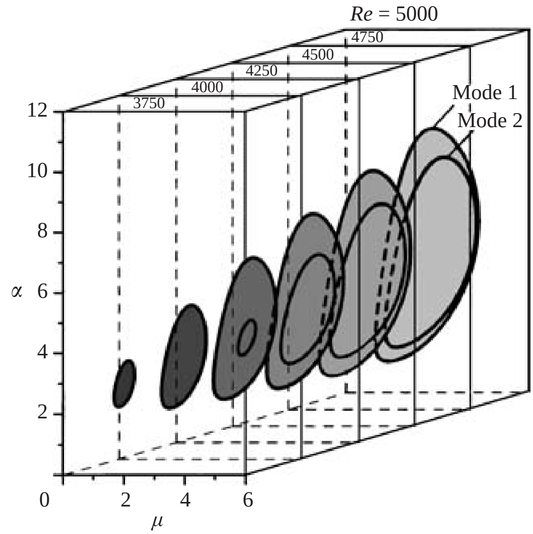

FIGURE 18. The neutral surfaces describing variation of the neutral stability conditions for the first and second instability modes for the amplitude of the channel divergence–convergence $S = 0.008$ as a function of the flow Reynolds number Re, the wavenumber α of the channel divergence–convergence and the vortex wavenumber μ. The flow is subject to the fixed mass constraint. The tips of the neutral surfaces define the global critical conditions ($Re_{g,cr}$, $\alpha_{g,cr}$, $\mu_{g,cr}$) for both modes.

gradient that is higher than the pressure gradient required to move the fluid at the same rate through a straight channel. We shall now enquire how the stability characteristics change when the flow develops with the fixed pressure gradient constraint. We would expect a decrease of the flow velocity resulting in flow stabilization. Figure 20 shows

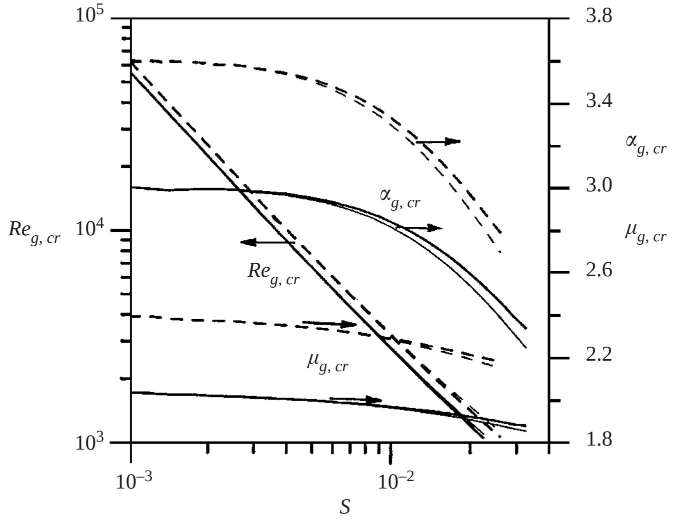

FIGURE 19. Variations of the global critical stability conditions $Re_{g,cr}$, $\alpha_{g,cr}$, $\mu_{g,cr}$ as a function of the amplitude S of the channel divergence–convergence. ——, First, and – – –, second instability modes. ——, The flow with fixed mass and ——, with fixed pressure constraints.

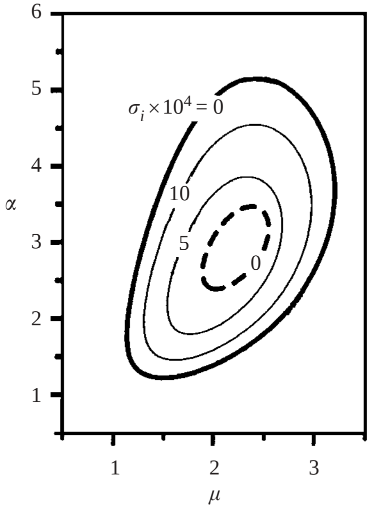

FIGURE 20. Amplification rates Imag(σ) of disturbances in the form of streamwise vortices induced in a flow with the Reynolds number $Re = 1500$ subject to the fixed pressure gradient constraint. The remaining conditions are as in figure 4. ——, First and – – –, second instability modes.

a stability diagram for both instability modes obtained under the same conditions as in figure 4 for the flow with fixed pressure gradient. Comparison of the neutral curves for both types of flow displayed in figure 21 demonstrates the expected flow stabilization due to the imposition of the fixed pressure gradient constraint and provides a quantitative measure of this change. The onset of the instability, as measured by the global critical Reynolds number, takes place under almost the same conditions for both types of flow as shown in figure 19. The small difference between $Re_{g,cr}$ increases with an increase of the wall amplitude S, with the flow with the fixed

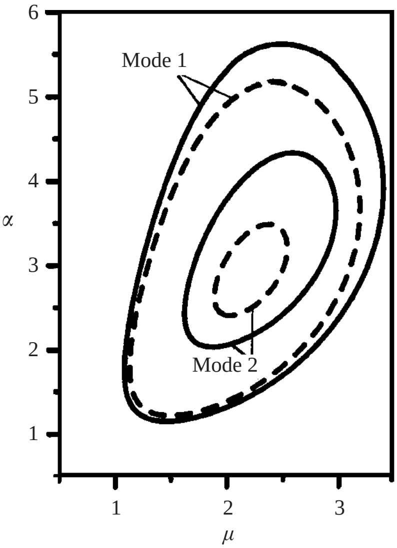

FIGURE 21. Neutral curves describing two modes of centrifugal instability in a flow subject to ——, the fixed mass constraint, and – – –, subject to the fixed pressure gradient constraint. The remaining conditions are as in figures 4 and 20.

pressure gradient commanding higher values of $Re_{g,cr}$. The increase of this difference is due to the progressively higher flow resistance associated with larger variations of the channel opening.

The final comments relate to the mechanism of the instability. It is argued that the instability is driven primarily by the centrifugal effect. The indirect evidence pointing in this direction has been discussed in the paper. We cannot, however, completely dismiss other possibilities, i.e. CL1 and CL2 mechanisms and parametric resonance. It is probable that all mechanisms act at the same time, while the evidence available suggests that the centrifugal effect is the most important.

This discussion is concluded by commenting on the turbulent flow. Presence of the channel divergence–convergence acts as a source of vorticity at the walls (figure 3*c*) and this could lead to an interesting dynamics of the flow. In addition, since the centrifugal effect is active regardless of the type of the flow, we may expect formation of streamwise vortices also in turbulent flows, which should affect the form of large structures.

5. Summary

Linear stability of a flow in a diverging–converging channel has been analysed. The analysis has been carried out in the context of a reference diverging–converging channel whose walls are described by simple sine functions. There are two parameters that completely describe the geometry of the reference diverging–converging channel, i.e. the amplitude S and the wavelength $\lambda = \alpha/2\pi$. The difference between the maximum and minimum channel openings is $8S$. The flow conditions are defined using the flow Reynolds number for a reference straight channel whose height is equal to the average height of the diverging–converging channel. Variations of channel geometry result in an increased flow resistance as compared to the straight channel. The flow in a diverging–converging channel may thus be allowed to develop with the same mass flux as the flow in the reference straight channel, or with the same pressure gradient. Both types of flow have been studied.

It has been shown, using linear stability theory, that flow in a divergent–convergent channel becomes unstable with respect to disturbances in the form of streamwise vortices. Analysis of the mean flow circulation and the disturbance flow field suggest that the instability is driven by centrifugal effect. Two modes of instability have been identified. The first mode (antisymmetric), which is more unstable, gives rise to a single layer of vortices filling in most of the channel interior. The second mode (symmetric) gives rise to two layers of vortices. These vortices are indirectly modulated in the streamwise direction by channel geometry through thin readjustment layers present at both walls. These layers have complex topology, especially in the diverging section of the channel.

For each amplitude S of the channel divergence–convergence there is a finite band of ‘active’ wavelengths $\alpha/2\pi$ of the channel divergence–convergence that gives rise to the instability. The instability amplifies streamwise vortices whose size is described by a continuous band of spanwise wavenumbers μ. The strength of the instability, as measured by the amplification rate, increases with the increase of the amplitude S of the channel divergence–convergence as well as with the increase of the flow Reynolds number Re. The range of the ‘active’ wavenumbers α and the range of the resulting vortices, as defined by the wavenumber μ, also increase with the increase of S and Re. Critical flow conditions leading to the onset of the instability can be found for each combination of S and α. The global critical conditions leading to the onset of the instability for the given amplitude S regardless of the wavelength of the channel divergence–convergence have been determined. The global critical Reynolds number decreases from $Re \approx 55 \times 10^3$ for $S \approx 10^{-3}$ to $Re \approx 10^3$ for $S \approx 0.02$. These results demonstrate that the centrifugal instability may dominate over the travelling wave instability at higher values of the amplitude S of the channel divergence–convergence. The flow that develops with the fixed mass flux constraint is slightly more unstable when compared with the flow driven by the fixed pressure gradient. This difference increases with the increase of the amplitude S of the channel divergence–convergence.

This work has been carried out with support of NSERC of Canada, de Havilland and Canadair. Drs J. Szumbarski and S. Krol wrote one of the codes used in the computations. The author would like to thank Dr S. Krol and M. Floryan for assistance in carrying out the required computations.

Appendix A

Coefficients $(w_k^j)_L$ can be evaluated from the following recurrence relation

$$\left(w_k^{j+1}\right)_L = 2\sum_{s=-\infty}^{s=+\infty} (A_k)_L \left(w_{k-s}^j\right)_L - \left(w_k^{j-1}\right)_L$$

with $(w_0^0)_L = 1$, $(w_k^0)_L = 0$ for $k \geqslant 1$, $(w_0^1)_L = (A_0)_L$ and $(w_k^1)_L = (A_k)_L$ for $k \geqslant 1$. Coefficients $(d_k^j)_L$ can be evaluated from the following recurrence relation

$$\left(d_k^{j+1}\right)_L = 2\sum_{s=-\infty}^{s=+\infty} (A_s)_L \left(d_{k+s}^j\right)_L - \left(d_k^{j-1}\right)_L + 2\left(w_k^j\right)_L$$

with $(d_k^0)_L = 0$ for $k \geqslant 0$, $(d_0^1)_L = 1$, $(d_k^1)_L = 0$ for $k \geqslant 1$, $(d_0^2)_L = 4(A_0)_L$ and $(d_k^2)_L = (A_k)_L$ for $k \geqslant 1$.

Appendix B

$$\mathrm{S}^{(m)} = \mathrm{D}^2 - k_m^2 - \mathrm{i}Re\,(t_m u_0 - \sigma) \tag{B 1}$$

$$\mathrm{T}^{(m)} = \left(\mathrm{D}^2 - k_m^2\right)^2 - \mathrm{i}Re\left[(t_m u_0 - \sigma)\left(\mathrm{D}^2 - k_m^2\right) - t_m \mathrm{D}^2 u_0\right] \tag{B 2}$$

$$\mathrm{C} = Re\mu \mathrm{D}u_0 \tag{B 3}$$

$$\mathrm{W}_u^{(m,n)} = \mu\left(\mathrm{i}f_v^{(n)}\mathrm{D} - t_m f_u^{(n)}\right) \tag{B 4}$$

$$\mathrm{W}_v^{(m,n)} = \mathrm{i}\mu \mathrm{D} f_u^{(n)} \tag{B 5}$$

$$\mathrm{W}_w^{(m,n)} = t_m\left(t_{m-n} f_u^{(n)} - \mathrm{i}f_v^{(n)}\mathrm{D}\right) \tag{B 6}$$

$$\mathrm{B}_u^{(m,n)} = -t_m^2 \mathrm{D} f_u^{(n)} + \mathrm{i}n\alpha k_m^2 f_v^{(n)} - t_m^2 f_u^{(n)}\mathrm{D} + \mathrm{i}t_m \mathrm{D} f_u^{(n)}\mathrm{D} + \mathrm{i}t_m f_v^{(n)}\mathrm{D}^2 \tag{B 7}$$

$$\mathrm{B}_v^{(m,n)} = \mathrm{i}k_m^2 t_{m-n} f_u^{(n)} + k_m^2 \mathrm{D} f_v^{(n)} + k_m^2 f_v^{(n)}\mathrm{D} + \mathrm{i}t_m \mathrm{D}^2 f_u^{(n)} + \mathrm{i}t_m \mathrm{D} f_u^{(n)}\mathrm{D} \tag{B 8}$$

$$\mathrm{B}_w^{(m,n)} = \mu\left(-t_{m-2n} f_u^{(n)}\mathrm{D} - t_{m-n}\mathrm{D} f_u^{(n)} + \mathrm{i}f_v^{(n)}\mathrm{D}^2\right) \tag{B 9}$$

$$\mathrm{E}_v^{(m,n)} = \mu\left(-\mathrm{D} f_u^{(n)} + \mathrm{i}n\alpha k_{m-n}^{-2} f_v^{(n)}\mathrm{D}^2\right) \tag{B 10}$$

$$\mathrm{E}_\theta^{(m,n)} = \mathrm{i}t_m f_u^{(n)} + \left(1 + n\alpha t_{m-n} k_{m-n}^{-2}\right) f_v^{(n)}\mathrm{D} \tag{B 11}$$

$$\begin{aligned}\mathrm{H}_v^{(m,n)} = {} & \mathrm{i}n\alpha k_{m-n}^{-2}(\mu^2 - t_m t_{m-n})\mathrm{D} f_u^{(n)}\mathrm{D} + k_m^2 k_{m-n}^{-2}(\mu^2 + t_{m-n}t_{m-2n}) f_v^{(n)}\mathrm{D} \\ & + \mathrm{i}k_{m-n}^{-2}\left(-k_{m-n}^2 t_m + 2n\alpha\mu\right) f_u^{(n)}\mathrm{D}^2 + k_{m-n}^{-2}\left(n\alpha t_m - k_m^2\right) f_v^{(n)}\mathrm{D}^3 \\ & + \mathrm{i}k_m^2 t_{m-2n} f_u^{(n)} + \mathrm{i}t_m \mathrm{D}^2 f_u^{(n)}\end{aligned} \tag{B 12}$$

$$\mathrm{H}_\theta^{(m,n)} = n\alpha\mu\left(2t_{m-n}k_{m-n}^{-2} f_u^{(n)}\mathrm{D} + k_{m-n}^{-2}(t_m + t_{m-n})\mathrm{D} f_u^{(n)} - \mathrm{i}k_m^2 k_{m-n}^{-2} f_v^{(n)} - \mathrm{i}k_{m-n}^{-2} f_v^{(n)}\mathrm{D}^2\right) \tag{B 13}$$

Appendix C

In the limit of zero waviness amplitude, (3.9) assumes the following form

$$\mathrm{S}^{(m)}\theta^{(m)} + \mathrm{C}g_v^{(m)} = 0, \tag{C 1}$$

$$\mathrm{T}^{(m)}g_v^{(m)} = 0. \tag{C 2}$$

Each pair of the above equations describes disturbances of periodicity $2\pi/m\alpha$ and $2\pi/\mu$ in the streamwise and spanwise directions, respectively. Equation (C 1) describes the so-called Squires modes and (C 2) describes the so-called Tollmien–Schlichting (TS) modes. In the case of streamwise vortices, i.e. $m = 0$, (C 1)–(C 2) reduce to the form

$$(\mathrm{D}^2 - \mu^2 + \mathrm{i}Re\sigma)g_u^{(0)} - Re\mathrm{D}u_0 g_v^{(0)} = 0, \tag{C 3}$$

$$(\mathrm{D}^2 - \mu^2)(\mathrm{D}^2 - \mu^2 + \mathrm{i}Re\sigma)g_v^{(0)} = 0. \tag{C 4}$$

The homogeneous part of (C 3) supplemented by the homogeneous boundary conditions at $y = \pm 1$ represents an eigenvalue problem describing Squires modes which has symmetric and asymmetric families of solutions. All symmetric solutions are attenuated and have the form

$$g_u^{(0)} = c_1 \cos\left[\left(\tfrac{1}{2}\pi + n\pi\right)y\right], \quad g_v^{(0)} = g_w^{(0)} = 0, \quad \sigma = -\mathrm{i}\left[\mu^2 + \left(\tfrac{1}{2}\pi + n\pi\right)^2\right]/Re, \tag{C 5}$$

where c_1 is an arbitrary constant. The least attenuated solution corresponds to $n = 0$. All asymmetric solutions are also attenuated and have the form

$$g_u^{(0)} = c_2 \sin(n\pi y), \quad \sigma = -\mathrm{i}(\mu^2 + n^2\pi^2)/Re, \tag{C 6}$$

where c_2 is an arbitrary constant. The least attenuated solution corresponds to $n = 1$.

Equation (C 4) supplemented by homogeneous boundary conditions represents an eigenvalue problem describing TS modes. The symmetric solutions, which are all attenuated, have the form

$$g_v^{(0)} = c_1\left[\cos(sy) - \frac{\cos(s)}{\cosh(\mu)}\cosh(\mu y)\right], \quad \sigma = -\mathrm{i}(s^2+\mu^2)/Re, \tag{C 7}$$

where s is a root of $s\sin(s)\cosh(\mu) + \mu\sinh(\mu)\cos(\mathrm{s}) = 0$ and c_1 is an arbitrary constant. The smallest positive roots that lead to the least stable solution have numerical values equal to 2.4809, 2.3271 for $\mu = 2$, 2.5, respectively. The asymmetric solutions have the form

$$g_v^{(0)} = c_2\left[\sin(sy) - \frac{\sin(s)}{\sinh(\mu)}\sinh(\mu y)\right], \quad \sigma = -\mathrm{i}(s^2+\mu^2)/Re, \tag{C 8}$$

where s is a root of $\sinh(\mu)s\cos(\mathrm{s}) \;-\mu\cosh(\mu)\sin(s) = 0$ and c_2 is an arbitrary constant. The smallest positive roots that lead to the least stable solutions have numerical values equal to 4.2591, 4.1659 for $\mu = 2$, 2.5, respectively.

REFERENCES

Amon, C. H., Guzman, A. M. & Morel, B. 1996 Lagrangian chaos, Eulerian chaos, and mixing enhancement in diverging–converging channel flows. *Phys. Fluids* **8**, 1192–1206.

Benmalek, A. & Saric, W. S. 1994 Effects of curvature variations on the nonlinear evolution of Görtler vortices. *Phys. Fluids* **6**, 3353–3367.

Bergless, E. A. & Webb, R. L. 1985 A guide to the literature on convective heat transfer augmentation. In *Advances in Heat Transfer – 1985*, The 23rd National Heat Transfer Conference, Denver, Colorado.

Cherukat, P., Na, Y., Hanratty, T. J. & McLaughlin, J. B. 1998 Direct numerical simulations of a fully turbulent flow over a wavy wall. *Theor. Comput. Fluid Dyn.* **11**, 109–134.

Craik, A. D. D. 1982 Wave-induced longitudinal-vortex instability in shear flows. *J. Fluid Mech.* **125**, 37–82.

Craik, A. D. D. & Leibovich, S. 1976 A rational model for Langmuir circulation. *J. Fluid Mech.* **73**, 401–426.

Coddington, E. A. & Levinson, N. 1965 *Theory of Ordinary Differential Equations*. McGraw-Hill.

De Angelis, V., Lombardi, P. & Banerjee, S. 1997 Direct numerical simulation of turbulent flow over a wavy wall. *Phys. Fluids* **9**, 2429–2442.

Dean, W. 1928 Fluid motion in a curved channel. *Proc. R. Soc. Lond.* A **121**, 402–412.

Drazin, P. G. & Reid, W. H. 1981 *Hydrodynamic Stability*. Cambridge University Press.

Fiebig, M. & Chen, Y. 1999 Heat transfer enhancement by wing-type longitudinal vortex generators and their application to finned oval tube heat exchanger elements. In *Heat Transfer Enhancement of Heat Exchangers* (ed. S. Kakac), pp. 79–105. Kluwer.

Floryan, J. M. 1986 Görtler instability of boundary layers over concave and convex walls. *Phys. Fluids* **29**, 2380–2387.

Floryan, J. M. 1991 On the Görtler instability of boundary layers. *Prog. Aerospace Sci.* **28**, 235–271.

Floryan, J. M. 1997 Stability of wall bounded shear layers with simulated distributed surface roughness. *J. Fluid Mech.* **335**, 29–55.

Floryan, J. M. 2002 Centrifugal instability of Couette flow over a wavy wall. *Phys. Fluids* **14**, 312–322.

Gong, W., Taylor, P. A. & Dörnbrack, A. 1996 Turbulent boundary-layer flow over fixed, aerodynamically rough two-dimensional waves. *J. Fluid Mech.* **312**, 1–37.

Görtler, H. 1941 Instabilität laminarer Grenzschichten an konkaven Wänden gegenüber gewissen dreidimensionalen Störungen. *Z. Angew. Math. Mech.* **21**, 250–252.

Gschwind, P., Regele, A. & Kottke, V. 1995 Sinusoidal wavy channels with Taylor–Görtler vortices. *Exp. Therm. Sci.* **11**, 270–275.

Guzmán, A. M. & Amon, C. H. 1994 Transition to chaos in converging–diverging channel flows: Ruelle–Takens–Newhouse scenario. *Phys. Fluids* **6**, 1994–2002.

Guzmán, A. M. & Amon, C. H. 1996 Dynamical characterization of transitional and chaotic regimes in converging–diverging channels. *J. Fluid Mech.* **321**, 25–57.

Herbert, T. 1977 Finite amplitude stability of plane parallel flows. *AGARD Conf. Proc.* **224**, 3.1–3.10.

Hudson, J. D., Dykhno, L. & Hanratty, T. J. 1996 Turbulence production in flow over a wavy wall. *Exp. Fluids* **20**, 257–265.

Leibovich, S. 1977 Convective instability of stably stratified water in the ocean. *J. Fluid Mech.* **82**, 561–585.

Leibovich, S. 1983 The form and dynamics of Langmuir circulation. *Annu. Rev. Fluid Mech.* **15**, 391–427.

Mendes, P. S. & Sparrow, E. M. 1984 Periodically converging–diverging tubes and their turbulent heat transfer, pressure drop, fluid flow, and enhancement characteristics. *J. Heat Transfer* **106**, 55–63.

Nakagawa, S. & Hanratty, T. J. 2001 Particle image velocimetry measurements of flow over a wavy wall. *Phys. Fluids* **13**, 3504–3507.

Nishimura, T., Kajimoto, Y. & Kawamura, Y. 1986 Mass transfer enhancement in channels with a wavy wall. *J. Chem. Engng Japan* **19**, 142–144.

Nishimura, T., Murakami, S., Arakawa, S. & Kawamura, Y. 1990*b* Flow observations and mass transfer characteristics in symmetrically wavy-walled channels at moderate Reynolds numbers for steady flow. *Intl J. Heat Mass Transfer* **33**, 835–845.

Nishimura, T., Ohori, Y., Kajimoto, Y. & Kawamura, Y. 1985 Mass transfer characteristics in a channel with symmetric wavy wall for steady flow. *J. Chem. Engng Japan* **18**, 550–555.

Nishimura, T., Ohori, Y. & Kawamura, Y. 1984 Flow characteristics in a channel with symmetric wavy wall for steady flow. *J. Chem. Engng Japan* **17**, 466–471.

Nishimura, T., Yano, K., Yoshino, T. & Kawamura, Y. 1990*a* Occurrence and structure of Taylor–Görtler vortices induced in two-dimensional wavy channels for steady flow. *J. Chem. Engng Japan* **23**, 697–703.

Orszag, S. A. & Patera, A. T. 1983 Secondary instability of wall-bounded shear flows. *J. Fluid Mech.* **128**, 347–385.

Patera, A. T. & Mikic, B. B. 1986 Exploiting hydrodynamic instabilities. Resonant heat transfer enhancement. *Intl J. Heat Mass Transfer* **29**, 1127–1138.

Perry, A. E. & Fairlie, B. D. 1974 Critical points in flow patterns. *Adv. Geophys.* B **18**, 299–315.

Phillips, W. R. C. 1998 On the nonlinear instability of strong wavy shear to longitudinal vortices. In *Nonlinear Instability, Chaos and Turbulence* (ed. L. Debnath & D. N. Riahi), pp. 251–273. Computer Mechanics, UK.

Phillips, W. R. C. & Wu, Z. 1994 On the instability of wave-catalysed longitudinal vortices in strong shear. *J. Fluid Mech.* **272**, 235–254.

Phillips, W. R. C., Wu, Z. & Lumley, J. L. 1996 On the formation of longitudinal vortices in a turbulent boundary layer over wavy terrain. *J. Fluid Mech.* **326**, 321–341.

Rayleigh, L. 1920 On the dynamics of the revolving fluids. *Scientific Papers*, vol. 6, pp. 447–453.

Saric, W. S. & Benmalik, A. 1991 Görtler vortices with periodic curvature. *Boundary Layer and Transition to Turbulence*, FED-114, ASME.

Szumbarski, J. & Floryan, J. M. 1999 A direct spectral method for determination of flows over corrugated boundaries. *J. Comput. Phys.* **153**, 378–402.

Taylor, G. 1923 Stability of viscous liquid contained between two rotating cylinders. *Phil. Trans. R. Soc.* A **223**, 289–293.

Wang, G. & Vanka, S. P. 1995 Convective heat transfer in periodic passages. *Intl J. Heat Mass Transfer* **38**, 3219–3230.